MULTICHANNEL COMMUNICATION BASED ON ADAPTIVE EQUALIZATION IN VERY SHALLOW WATER ACOUSTIC CHANNELS

TAN BIEN AIK
(B.Eng. (Hons.), NUS)

A THESIS SUBMITTED

FOR THE DEGREE OF MASTER OF ENGINEERING

DEPARTMENT OF ELECTRICAL AND COMPUTER ENGINEERING

NATIONAL UNIVERSITY OF SINGAPORE

ACKNOWLEDGEMENTS

The author would like to thank his supervisors, Dr Mehul Motani, who is an Assistant Professor in Electrical and Computer Engineering department at the National University of Singapore, Associate Professor John R. Potter, who is an Associate Director of Tropical Marine Science Institute at the National University of Singapore and Dr. Mandar A. Chitre, who is the Deputy Head of Acoustic Research Laboratory at the National University of Singapore, for their time and invaluable guidance throughout the progress of this thesis.

The author wishes to thank DSO National Laboratories for making the data available. The author would also like to thank his DSO colleagues – Mr Koh Tiong Aik, Mr Quek Swee Sen and Mr Zhong Kun for their help with the sea trial experiments and data transmissions/acquisitions and in addition, Mr Quek Swee Sen again for the help and contributions for the turbo product code notes and MATLAB® functions that were provided for in this thesis.

This thesis will not be possible without the understanding and support from the author's family and Miss Nina Chun.

TABLE OF CONTENTS

SUMMARY

Very shallow water acoustic communication channels are known to exhibit fading due to time-varying multipath arrivals. This is further complicated by impulsive snapping shrimp noise that is commonly present in warm shallow waters. Channel measurements and analyses were done to study the local shallow water characteristics. These measurements had helped verify and set the communication channel model and adaptive receivers presented in this thesis. This thesis also presents results from the use of single-carrier differential phase shift keying (DPSK) modulation. The receiver designs in the simulation and trial data analysis were based on combinations of least mean square (LMS) and recursive least square (RLS) algorithms with adaptive linear equalizer (LE) and decision feedback equalizer (DFE). In addition, multichannel combining (MC) and forward error correction (FEC) scheme such as turbo product codes (TPC) were employed to improve performance by removing correctable errors. Performance results based on simulated data as well as for real data collected from the sea were also presented.

LIST OF TABLES

LIST OF FIGURES

LIST OF SYMBOLS AND ABBREVIATIONS

Symbols

L	Horizontal distance between the transmitter and receiver
t	Continuous time index
a	Depth of transmitter
b	Depth of receiver
A	A coefficient associated with the Lyords mirror effects
h	Bottom depth
D	Distance traveled by direct ray in Ray Theory
n	Order of reflections
SS_n	n^{th} signal path, in distance, which makes the first and last boundary reflection with the surface
SB_n	n^{th} signal path, in distance, which makes the first boundary reflection with the surface and last boundary reflection with the bottom
BS_n	n^{th} signal path, in distance, which makes the first boundary reflection with the bottom and last boundary reflection with the surface
BB_n	n^{th} signal path, in distance, which makes the first and last boundary reflection with the bottom
c	Underwater sound velocity
t_D	Arrival time of direct arrival
t_{SS_n}	Arrival time of SS_n
t_{SB_n}	Arrival time of SB_n
t_{BS_n}	Arrival time of BS_n
t_{BB_n}	Arrival time of BB_n
τ_{SS_n}	Propagation delay of SS_n relative to the direct arrival
τ_{SB_n}	Propagation delay of SB_n relative to the direct arrival
τ_{BS_n}	Propagation delay of BS_n relative to the direct arrival

τ_{BB_n}	Propagation delay of BB_n relative to the direct arrival
k_c	A coefficient associated with the angle of arrival of the acoustic ray at the receiver
Ψ	Angle of arrival of the acoustic ray at the receiver
L_s	Spreading loss of an omni-directional acoustic pressure wave
$\beta_{dB/km}$	Frequency dependent attenuation loss in decibels per kilometre
L_A	Attenuation factor
f	Acoustic frequency in kHz
f_c	Acoustic carrier frequency in kHz
f_T	A coefficient associated with the frequency dependent attenuation loss
T_w	Temperature of water in degrees Fahrenheit
T_{degC}	Temperature of water in degrees Celsius
$\tilde{r}_s$	Surface reflection loss
$\tilde{r}_b$	Bottom reflection loss
f_1	A coefficient associated with the surface reflection loss
f_2	A coefficient associated with the surface reflection loss
ρ	Density
m_ρ	Ratio of bottom density to water density
n_c	Ratio of sound velocity in water to sound velocity in bottom
θ	Grazing angle of the incident acoustic ray with the bottom
R_{SS_n}	Combined reflection loss of a n^{th} order *SS* acoustic ray
R_{SB_n}	Combined reflection loss of a n^{th} order *SB* acoustic ray
R_{BS_n}	Combined reflection loss of a n^{th} order *BS* acoustic ray
R_{BB_n}	Combined reflection loss of a n^{th} order *BB* acoustic ray
x(t)	Transmitted Signal

$r(t)$	Received Signal
α	Combined transmission loss of the acoustic ray
$P(\tau)$	Average power delay profile
$E_i(\tau)$	ith Power delay profile
$h(\tau)$	Bandpass impulse response
T_m	Excessive delay spread
σ_τ	Root mean squared delay spread
T_s	Symbol period
B_c	Coherence bandwidth
f_d	Doppler spread
T_o	Coherence time
$S(v)$	Scattering function
$S(f)$	Doppler spectrum
$\rho(\Delta t)$	Space time correlation function
k	Discrete time index
$a(k)$	Original bit sequence
$d(k)$	Differentially encoded bit sequence
$z(k)$	Differentially decoded soft output sequence
$r(k)$	Complex baseband received signal
$\tilde{a}(k)$	Estimated original bit sequence
$e(k)$	Error signal
$y(k)$	Adaptive filter output
$\mathbf{r}(2k)$	Adaptive filter input vector
$b(k)$	Training Signal/Tracking Signal
$\mathbf{f}_f(k)$	Feed forward fitler tap coefficient vector
μ_{ff}	Feed forward adaptation step size

N	Number of filter taps
N_f	Number of feed forward filter taps
N_b	Number of feed back filter taps
μ_{fb}	Feed back tap adaptation step size
b(k)	Feed back vector
$\mathbf{f}_b(k)$	Feed back fitler tap coefficient vector
δ	A coefficient associated with RLS algorithm
λ	Forgetting factor of the RLS algorithm
$\mathbf{\Phi}^{-1}$	A $N_f + N_b$ square matrix of the RLS algorithm
k_u	A coefficient associated with the TPC encoder structure
n_d	A coefficient associated with the TPC encoder structure
$c_e(k)$	Channel effects sequence
$d_c(k)$	Differentially encoded TPC codeword
$a_c(k)$	TPC Codeword
$y_c(k)$	Adaptive filter output of differentially encoded TPC codeword
ϕ	Phase offset of adaptive filter output
$n(k)$	Noise signal component of adaptive filter output

Abbreviations

BER	Bit Error Rate
BPSK	Binary Phase Shift Keying
DBPSK	Differential Binary Phase Shift Keying
CDF	Cumulative Distribution Funtion
CW	Continuous Wave
DFE	Decision Feedback Equalizer
DPSK	Differential Phase Shift Keying
FIR	Finite Impulse Response
FER	Frame Error Rate
GPS	Global Positioning System
IIR	Infinite Impulse Response
ISI	Inter Symbol Interference
LE	Linear Equalizer
LMS	Least Mean Square
LOS	Line Of Sight
MC	Multichannel Combining
MIMO	Multiple Input Multiple Output
MPDP	Multipath Power Delay Profile
MMSE	Minimum Mean Square Error
MSE	Mean Square Error
OFDM	Orthogonal Frequency Division Multiplexing
PAPR	Peak to Average Power Ratio
PC	Personal Computer
PDF	Probability Density Function
PN	Pseudo Noise
RLS	Recursive Least Square

RMS	Root Mean Square
SISO	Soft-Input-Soft-Output
SNR	Signal to Noise Ratio
TPC	Turbo Product Code

CHAPTER 1 INTRODUCTION

1.1 Literature Review

The recorded history of underwater acoustics dates back to 1490 when Leonardo da Vinci wrote [1]: “If you cause your ship to stop, and place the head of a long tube in the water and place the outer extremity to your ear, you will hear ships at a great distance from you.” This remarkable disclosure has helped to develop many modern underwater acoustic technologies for civil and military applications. These include fishing, submarine, bathymetric and side scan SONARs, echo sounders, Doppler velocity loggers, acoustic positioning systems, and more importantly, underwater acoustic communications system, which is of considerable interest in today’s research. The technological advent of underwater explorations and sensing applications such as unmanned/autonomous underwater vehicles (U/AUVs), offshore oil and gas operations, ocean bottom monitoring stations, remote mine hunting and underwater structure inspections have driven the need for underwater wireless communications. Sound transmission is the single most effective means of directing energy transfer over long distances in sea-water. Radio-wave propagation is ineffective for this purpose because all but the lowest usable frequencies attenuates rapidly in the conducting sea water. And, optical propagation is subjected to scattering by suspended material in the sea [2, pp. 1.1-1.2].

What do we know about the shallow acoustic communication channel and how do we characterize it? Very shallow water acoustic communication channel is generally characterized as a multipath channel due to the acoustic signal reflections from the surface and the bottom of the sea [3]. However, it is also well known that the shallow water channel exhibits time varying multipath fading [4-6]. Time variability in the channel response results from a few underwater phenomena. Random signal fluctuation due to micro-paths [7] is one of the phenomenon but it is more dominant in

deep oceans where there are stronger presence of internal waves and turbulence [8]. For shallow waters, micro-paths of each signal path are less dominant in contributing to random signal fluctuation and these micro-paths are generated from the acoustic scattering caused by small inhomogeneities in the medium and other suspended scatterers. In addition, surface scattering due to surface waves and random Doppler spreading of surface reflected signals due to motion of reflection point may have added to the channel's time variability for shallow water [4]. As a result, the signal multipath components undergo time-varying propagation delays, resulting in signal fading. This is further complicated by impulsive snapping shrimp noise that is commonly present in Singapore's warm waters [6, 9]. Propagation in shallow water may be modeled using Ray theory, Normal mode, Fast Field or Parabolic Equation method [3, p. 223]. For high frequencies in shallow water, Ray theory is one such model that is adequate to describe the multipath structure of the channel [3]. Zielinksi [10] presented a simple and practical time invariant shallow water ray model for acoustic communications. Yeo [11] extended Zielinski's work and verified experimentally that the model is appropriate for shallow water channels. Later, Geng and Zielinski [12] also claimed that the underwater channel is not a fully scattering channel where there may be several distinct eigenpaths linking the transmitter and receiver. Each distinct eigenpath may contain a dominant component and a number of random sub-eigenpath components. Recently, Gutierrez [13] also proposed an eigenpath model with random sub-eigenpath components. As there were a lack of sea experimental analysis to verify the models from [12, 13], this thesis adopted the model in [10]. As for time variability, Chitre [6, 14] had proposed using Rayleigh fading model with some local sea trial data analyses backing (very short distances < 100m). This is similar to the Rayleigh fading model that is commonly used in radio communications [15, pp. 222-223]. The model

presented in this thesis is based on [10] and its time variability effect is based on [6, 14, 15].

One of the earliest underwater communication systems was a submarine's underwater telephone developed by the United States in 1945 [16]. It can be used for several kilometres and employed single side band modulation in the band of 8-11kHz. In recent years, significant advancements have been made in the development of underwater acoustic digital communications with improved communication distance and data throughput [4, 5]. The main performance limitations of the underwater acoustic communications are channel phase stability, available bandwidth and channel impulse response fluctuation rate [5]. To overcome these difficulties, the design of commercially available underwater modems has mostly relied on the use of robust non-coherent and spread spectrum modulation techniques. Unfortunately, these techniques were known to be bandwidth inefficient and it will be difficult to achieve high data rates in the severely band limited underwater acoustic channel ~ typically, less than 1 kilobits per second (kbps) or about 0.02 to 0.2 bits/Hz efficiency for distances between one to two kilometers (according to some COTS underwater modem specifications). Some of these commercial modems had been deployed in our local, very shallow waters of depths of less than 30m with impulsive noise. These modems, that had worked well in other channels, performed poorly by having to set its baud rate to the lowest in order to achieve reliable communications (~100-300bps) for distances up to 2km. On the other hand, research focus had shifted to phase-coherent modulation techniques. The most noticeable was the coherent detection of digital signals at 30-40kbps for a time varying 1.8km shallow water channel presented by Stojanovic [4] in 1997. These advanced techniques have yet to be used in commercially available acoustic modems.

Recently, channel measurements at medium frequency ranges (9-28kHz) in very shallow water (15-30m) at distances ranging from 80m to 2.7km in the coastal sea of Singapore have shown that it is possible to reliably send high data rate communication signals [17]. It also highlighted that it is more difficult to obtain the same high data rates (that is achievable at longer distances[1]) at shorter distances due to increased delay and Doppler spreads. These were supported by some local development work on orthogonal frequency division multiplexing (OFDM) by [14, 18, 19]. OFDM has been successful in achieving higher data rates in multipath environment without the help of channel equalization as it avoid inter symbol interference (ISI) effects by sending multiple low rate sub-carrier signals simultaneously with time guards called cyclic prefix and postfix. In [19], the OFDM modem had a maximum data rate of 10kbps at 1700m but it had to step down its data rates as the distance reduces. This is because using OFDM alone (without equalization) to combat the multipath effect often force system designers to reduce data rate in more severe time-dispersive channels. The increase in delay spread effectively increases the time guards required. Despite this, their frequency diversity or multi-carrier modulation techniques have produced reliable and higher data rates when compared to some of the COTS modems available. However, OFDM do have some drawbacks. High peak to average power ratio (PAPR) in OFDM transmission is inherent and it will need special coding scheme to reduce the PAPR. OFDM also have training/tracking problems in adaptive equalization of its low rate sub-carrier signals if it wants to maintain high bit rates for a wider range of delay spreads. Finally, in mobile underwater communications, a more complicated Doppler correction algorithm for the multi-carrier system is needed when compared to one in a single carrier system. Some

[1] As the bottom depth for the sea trial experiments and simulation does not vary much (~15m to 30m), long distances mentioned here usually meant that the range – depth ratio is large (larger than 30).

other possible techniques/enablers for high data rate are single carrier modulation with adaptive equalization [8, 20-22], adaptive multichannel combining [20, 23-25] and multiple input multiple output (MIMO) / Time Reversal (TR) system [26-28]. MIMO system leverages on space-time diversity to increase data rate. In a MIMO wireless link, the data stream is broken into separate signals and sent through separable multipath channels in space. In underwater, MIMO system, such as in [26, 27], may require the projector and receiver arrays to span across a few meters or even the water column in order to exploit the multipath channel. This will result in making the MIMO system setup too bulky. While adaptive equalization and multichannel combining has not been explored in our local waters, they do not suffer the drawbacks of OFDM and still remain physically compact unlike MIMO. The disadvantage of single carrier - multichannel communication with adaptive equalization is the higher order of complexity of implementation when compared to multi-carrier - OFDM alone. Therefore this thesis will experiment the sea data with single carrier adaptive equalization and multichannel combining to provide consistent high and reliable data rate over the challenging channels described above. Single carrier DPSK was chosen as it does not require an elaborate method for estimating the carrier phase.

Apart from using MIMO to exploit the multipath structure of the underwater channel, can we exploit some other knowledge about the channel in communication signal processing? Channel measurements in [17] had shown that the shallow water multipath power delay profiles were sparse and these were prevalent in short distances. Some proposed exploits in sparse multipath channels were found in [29, 30]. The length of adaptive equalizer in underwater communications was known to be excessively long due to long delay spreads. This poses three problems: an increase in computational complexity, slower convergence rate and the increased noise in channel

equalization. In Kocic [29], the aim of the work was to reduce the complexity of the adaptive equalizer by exploiting the sparse multipath channel. As the threshold to de-activate taps in [29] was considered high, the effect would be a significant reduction in computational load with negligible loss in performance. Similarly, having large number of filter taps also slows down the convergence process of the equalizer as the step size has to be reduced to guarantee stability. To address the slow convergence problem in fast fading and long delay channels, Heo [30] proposed channel estimate based tap initialization and sparse equalization to hasten the convergence process. This result in faster initial and nominal convergence and a one-two decibel increase in signal to noise ratio (SNR), when compared to the conventional approach. This thesis will explore sparse equalization to reduce noise in the estimate of inverse channel so as to improve the BER performance of the equalizer.

1.2 Contributions

Channel measurements and analyses were done to study the local shallow water characteristics. These measurements had helped verify the communication channel model presented in this thesis. The reader may also find the channel measurement sections useful in designing communication system. This thesis had presented results from the use of single-carrier differential phase shift keying (DPSK) modulation. The receiver designs in sea trial data analyses were based on combinations of least mean square (LMS) and recursive least square (RLS) algorithms with adaptive linear equalizer (LE) and decision feedback equalizer (DFE). The LE-LMS receiver was simulated using the channel model simulator for all distances tested and the simulated results were approximately matched to the ones obtained from the sea trial. In order to achieve reliable communications, multichannel combining (MC) and forward error correction (FEC) scheme such as turbo product codes (TPC) were

employed to improve performance by removing correctable errors. These results a detailed performance analyses of different equalizers and adaptation algorithms over a range of communication distances (80m to 2740m). In addition, sparse equalization had been explored in order to exploit the sparse channel and reduce the noise in the inverse channel estimate of adaptive equalizers. Performance results were based on real data collected from the sea.

1.3 Thesis Outline

The thesis is organised into four main chapters. The first chapter presents the literature review. The first half of chapter two presents a propagation channel model that is suitable for our shallow water geophysics. Remaining parts of the second chapter attempts to characterize underwater communication channel as well as to obtain the parameters for channel model simulations and adaptive receivers. Chapter three verifies the channel simulator, discussed in chapter one and two, by digital communication performance analysis via simulation as well as sea trial data. Finally, in chapter four, sea trial and some simulated performance of adaptive equalization algorithms, sparse equalization, multichannel combining and channel coding were presented.

CHAPTER 2 UNDERWATER ACOUSTIC CHANNEL

An underwater acoustic channel is characterized as a multipath channel due to signal reflections from the surface and the bottom of the sea. Because of surface wave motion, the signal multipath components undergo time varying propagation delays that results in signal fading. In addition, there is frequency dependent attenuation which is approximately proportional to the square of the signal frequency. The sound velocity is nominally about 1540m/s but the actual value will vary either above or below the nominal value depending on the temperature, salinity and hydrostatic pressure at which the signal propagates. Ambient ocean acoustic noise is caused by shrimp, fish, and various mammals. Unfortunately, ocean ambient noise also includes man made acoustic noise such as seismic surveys, ship traffic and land reclamation. When sound propagates underwater, it undergoes a number of effects. The following sections will briefly explain these effects.

2.1 Propagation Model

There are many methods of multipath modeling. Figure 2.1 shows the general techniques used [3] to solve the Helmholtz (Wave) equation in acoustic propagation modeling. For shallow water channel, the acoustic characteristics of both the surface and bottom of the channel are important determinants of the sound field due to repeated reflections from both the surface and bottom. Propagation in shallow water may be modelled using Ray theory, Normal mode, Fast Field or Parabolic Equation method (see Figure 2-1 and Table 2-1). For high frequencies in shallow water, Ray theory is one such model that is adequate to describe the multipath structure of the channel [3, p. 223]. High frequency here refers to having acoustic wavelength that is smaller than the bottom depth (preferably less than 0.1 of the bottom depth). For this

research work, the depth is roughly 30m maximum, the sound velocity is typically 1540 m/s and the carrier frequency is typically at 18.5 kHz for medium range communication. Thus the wavelength to bottom depth ratio is 2.77 $x10^{-3}$.

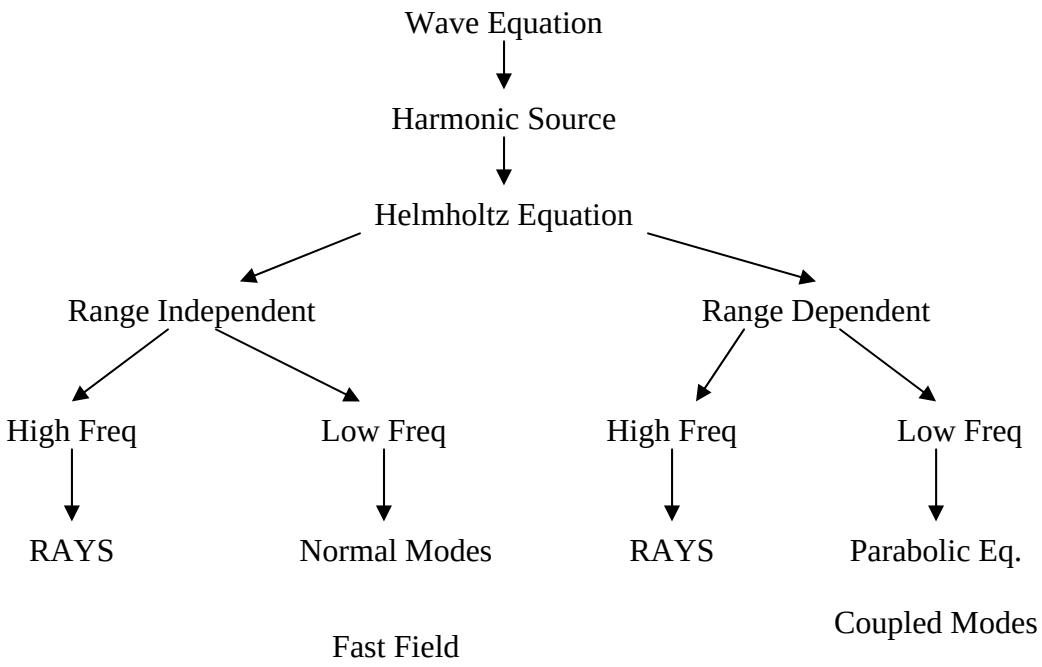

Figure 2-1. Methods to solve the Helmholtz equation

Table 2-1. Applicability of propagation models [3]

	Shallow Water				Deep Water			
	LF		HF		LF		HF	
	RI	RD	RI	RD	RI	RD	RI	RD
Ray Trace								
Normal Mode								
Fast Field								
Parabolic Equation								

LF-Low frequency HF-High Frequency RI-Range Independent RD-Range Dependent

Legend -Good -Neutral -Inappropriate

Zielinski [10] propose a multipath model for shallow waters shown in Figure 2-2. The channel model is characterized by Ray theory (simplified with constant sound velocity profile and constant bottom depth assumptions) and extending it to a

multipath expansion for a series of reflections resulting in multipath arrival at the receiver. Figure 2-2 is slightly different from [10] so that *a*, and *b* now represent the transmitter's and receiver's depth instead of its height which is not so conventional. As such, the equations for path lengths, angle of arrivals and delays are re-stated here for clarity.

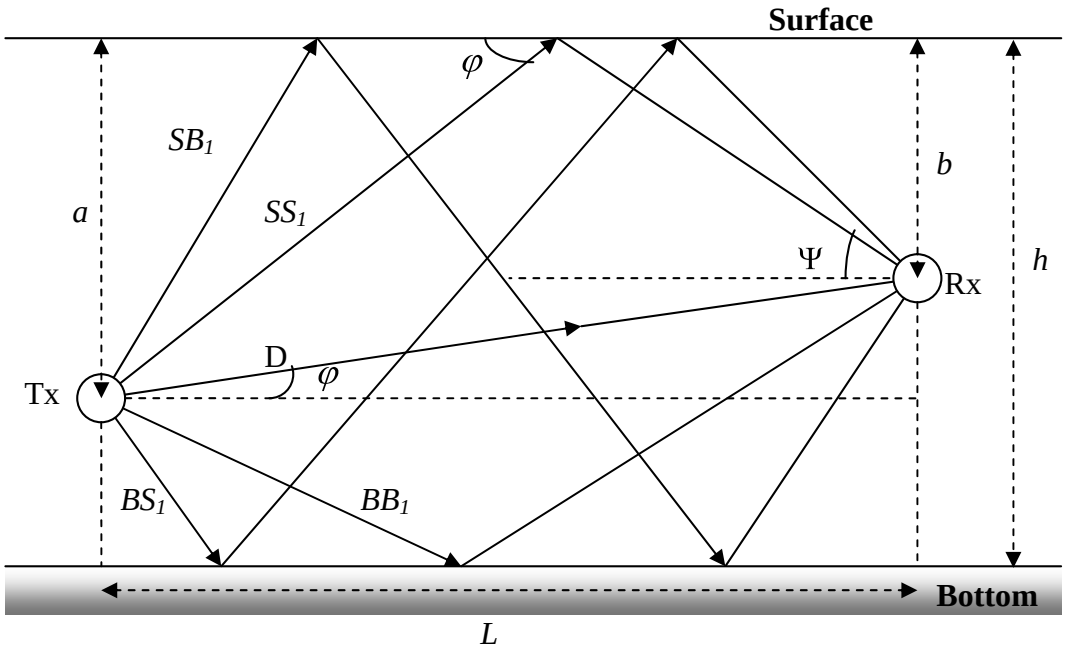

Figure 2-2. Shallow water multipath model from [10]

The transmitted signal path can be classified as direct path D or multipath. Multipaths are classified into four types and order of reflections, *n*. For example, notation SS_1 will denote multipath signal which make the first and last boundary reflection with the surface with first order of reflection as shown in the figure. The channel can be visualized using Lyords mirror effect [31] to compute the signal path length, angle of arrivals and delays.

The length of each signal path shown in Figure 2-2 is

$$\sqrt{L^2 + A^2}\ . \qquad \textbf{(Eq. 2-1)}$$

The angle of arrival of the acoustic ray at the receiver is given by

$$\Psi = k_c \times \tan^{-1}\left(\frac{A}{L}\right) \qquad \textbf{(Eq. 2-2)}$$

In the above

$$\begin{array}{lll} A = a - b & k_c = -1 & \text{for } D \\ A = 2h(n-1) + a + b & k_c = 1 & \text{for } SS_n \\ A = 2nh + a - b & k_c = -1 & \text{for } SB_n \\ A = 2nh - a + b & k_c = 1 & \text{for } BS_n \\ A = 2nh - a - b & k_c = -1 & \text{for } BB_n \end{array} \qquad \textbf{(Eq. 2-3)}$$

Therefore the length of signal path can be computed by substituting Eq. 2-3 into Eq. 2-1.

$$\begin{array}{ll} D = \sqrt{L^2 + (a-b)^2} & \text{for } D \\ SS_n = \sqrt{L^2 + \left[2h(n-1) + a + b\right]^2} & \text{for } SS_n \\ SB_n = \sqrt{L^2 + (2nh + a - b)^2} & \text{for } SB_n \\ BS_n = \sqrt{L^2 + (2nh - a + b)^2} & \text{for } BS_n \\ BB_n = \sqrt{L^2 + (2nh - a - b)^2} & \text{for } BB_n \end{array} \qquad \textbf{(Eq. 2-4)}$$

The difference in arrival time between the direct path and the multipath signals can be written as follows:

$$\tau_{SS_n} = t_{SS_n} - t_D = \frac{SS_n - D}{c} \qquad \textbf{(Eq. 2-5)}$$

where t_D and τ_{SS_n} are arrival times of direct and SS_n paths and c is the sound velocity. Similarly, we have:

$$\tau_{SB_n} = t_{SB_n} - t_D = \frac{SB_n - D}{c} \qquad \textbf{(Eq. 2-6)}$$

$$\tau_{BS_n} = t_{BS_n} - t_D = \frac{BS_n - D}{c} \qquad \textbf{(Eq. 2-7)}$$

$$\tau_{BB_n} = t_{BB_n} - t_D = \frac{BB_n - D}{c} \qquad \textbf{(Eq. 2-8)}$$

2.1.1 Sound Velocity

Because of the isovelocity assumption (constant sound velocity over all depths), the rays depicted here are straight. This is a fair assumption as most sound velocity profile recorded in our shallow water showed less than 1m/s variation in velocity over depth. This is reasonable as there is little variation of temperature over depth. Additionally, tidal currents usually establish a good mixing of salinity that lead to isovelocity conditions. A typical sound velocity profile is shown in Figure 2-3.

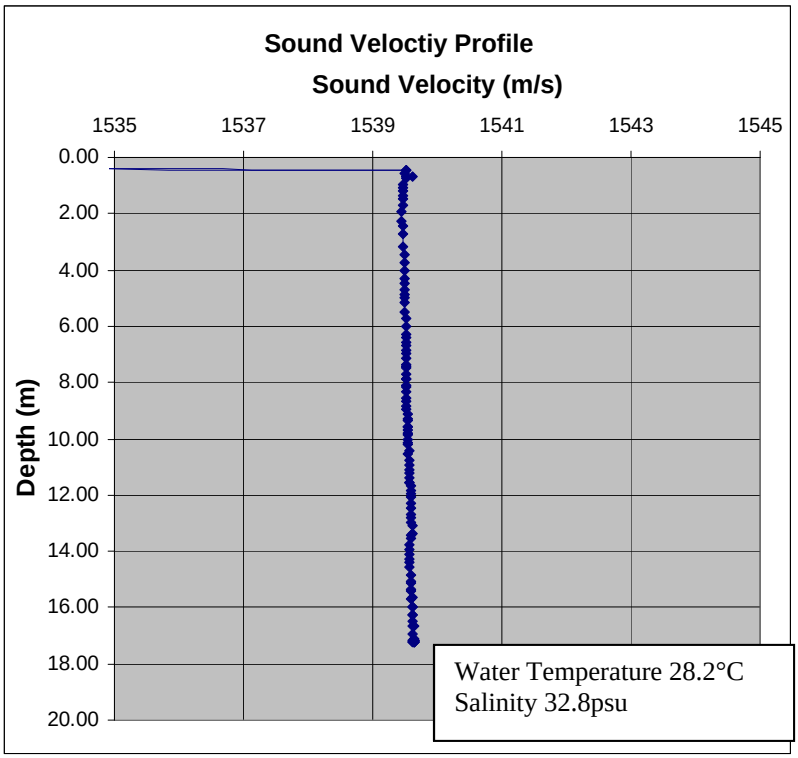

Figure 2-3. Typical sound velocity profile in local waters

If the sound velocity over depth changes considerably, rays bending will occur and the rays will always bend towards regions of lower propagation speed. The sound velocity of 1540m/s will be assumed here in this thesis.

2.1.2 Spreading Loss

When sound pressure wave propagates outward from an omni-directional source, it decreases in acoustic intensity, due to the increasing surface area of the outward propagating wavefront and this constitutes spreading loss (SL). There are two estimates of spreading loss, namely spherical or free field spreading loss and cylindrical spreading loss [2]. The amplitude loss along a signal path length D will then be:

Spherical Spreading $$L_S(D) = \sqrt{\frac{1}{D^2}} = \frac{1}{D}$$ **(Eq. 2-9)**

Cylindrical Spreading $$L_S(D) = \sqrt{\frac{1}{D}} = \frac{1}{\sqrt{D}}$$ **(Eq. 2-10)**

Cylindrical spreading loss is valid in non-coherent processing where all the signal paths are lumped. However, for coherent processing, where each path's contribution is considered, each path has to assume spherical spreading. In this thesis, spherical spreading loss is adopted.

2.1.3 Attenuation Loss

Spreading loss constitute part of transmission loss. When the frequency of transmission is high or broadband, or if the distance of transmission is long (typically tens of kilometers), frequency dependent volume absorption becomes significant and is termed attenuation loss. There are several models available for different frequency range and channel types [32]. The model adopted here is the Hall-Watson Model [32]. Most of the other models are not suitable as they are suited for a lower temperature range, or the frequency range is rather limited. The Hall-Watson model is picked due to its adequate frequency range of 500Hz to 50kHz and unrestricted temperature range. The absorption coefficient, $\beta_{dB/km}$, is a function of frequency and temperature [32]:

$$\beta_{dB/km} = \frac{1000}{914.4}\left[\begin{array}{l} 1.776 f^{1.5} + \\ f^5\left(\frac{0.65053 f_T}{f^2 + f_T^2} + \frac{0.026847}{f_T}\right) \end{array}\right] \frac{1}{\left(32.768 + f^3\right)} \qquad \textbf{(Eq. 2-11)}$$

where f is the frequency in kHz and $f_T = 21.9 \times 10^{\left(\frac{30T+102}{5T+2297}\right)}$

We will assume f to be the carrier frequency of the signal.

T_w is the water temperature in degrees Fahrenheit (T_w =32 + 1.8T_{degC}).

A plot of the absorption coefficient against the frequency for temperature of 29˚c and Salinity of 35 ppt (Singapore's typical waters condition) is shown in Figure 2-4.

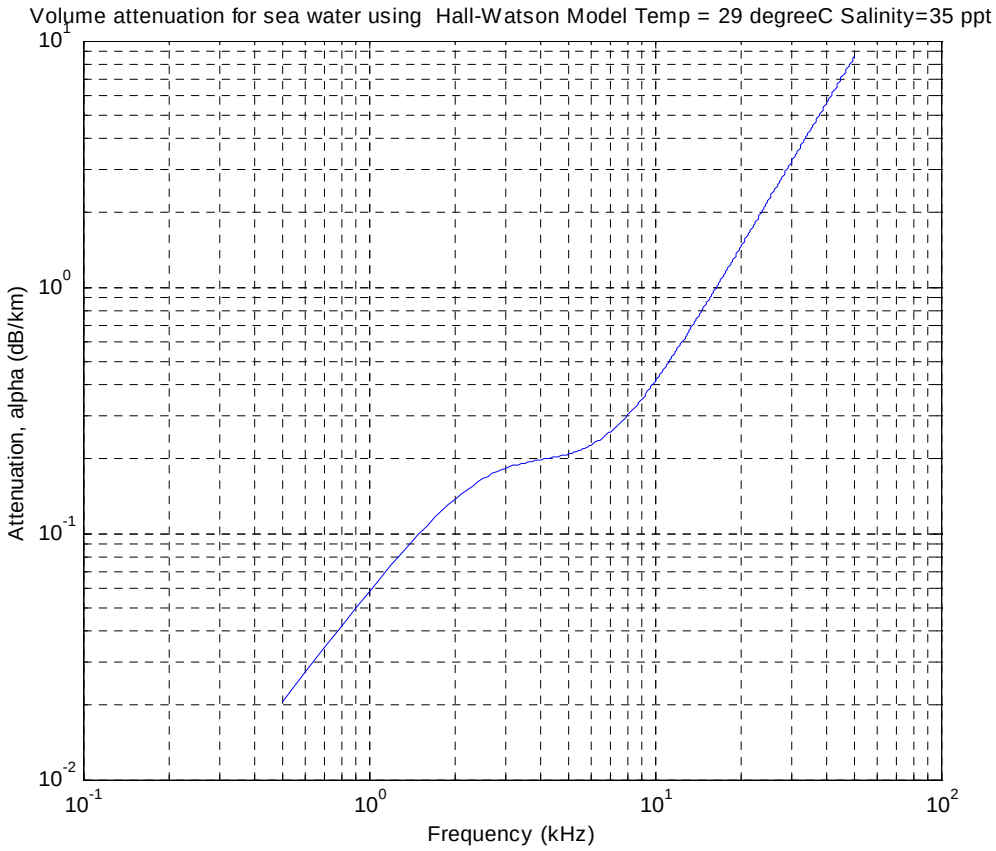

Figure 2-4. Volume attenuation for sea water at temperature of 29˚c given by the Hall-Watson formula

Therefore the attenuation factor can be computed for each signal path length D as:

$$L_A(D) = 10^{\left(\frac{D}{1000}\beta\right)/20} \qquad \textbf{(Eq. 2-12)}$$

2.1.4 Surface Reflection Loss

The acoustic pressure decrease for each reflection on the surface and it depends on the grazing angle. The complex surface reflection coefficient, $\tilde{r}_s$, is evaluated empirically using the Beckmann-Spizzichino model in the form proposed by Coates [33].

Beckmann-Spizzichino surface reflection loss –

$$\left|\tilde{r}_s\right| = \left| \sqrt{\left[\frac{1+\left(\frac{f_c}{f_1}\right)^2}{1+\left(\frac{f_c}{f_2}\right)^2}\right]} \Big/ 10^{\frac{\left(1+\frac{(90-w)}{60}\right)\left(\frac{\theta}{30}\right)^2}{20}} \right| \qquad \textbf{(Eq. 2-13)}$$

where $f_1 = \sqrt{10 f_2}$, $f_2 = 378 w^{-2}$ and w is wind speed knots, f_c is the carrier frequency in kHz, and $\theta = \Psi$ is the ray grazing at an angle to the surface. Considering the -180˚ phase shift due to the reflection from the sea surface,

$$r_s = -\left|\tilde{r}_s\right| \qquad \textbf{(Eq. 2-14)}$$

2.1.5 Bottom Reflection Loss

When the incident acoustic ray strike on the bottom, depending on the grazing angle, some of the acoustic energy will penetrate into the bottom as refracted ray and the remaining acoustic ray gets reflected back into sea water medium. Let ρ_1 and c_1 be the density and sound speed of sea water. Let ρ_2 and c_2 be the density and sound speed of the bottom. The bottom reflection loss can be evaluated using the Rayleigh model [34].

$$r_b = \left| \frac{m_\rho \sin\theta - \sqrt{\left(n_c^{\,2} - \cos^2\theta\right)}}{m_\rho \sin\theta + \sqrt{\left(n_c^{\,2} - \cos^2\theta\right)}} \right| \qquad \textbf{(Eq. 2-15)}$$

where $m_\rho = \frac{\rho_2}{\rho_1}$ and $n_c = \frac{c_1}{c_2}$ and $\theta = \Psi$ is the grazing angle of the acoustic incident ray with the bottom.

Therefore the combined repeated surface and/or bottom reflection for any type of multipath of order *n* are given by:

$$R_{SS_n} = r_s^{\,n} r_b^{\,n-1} \quad \textbf{(Eq. 2-16)}$$

$$R_{SB_n} = r_s^{\,n} r_b^{\,n} \quad \textbf{(Eq. 2-17)}$$

$$R_{BS_n} = r_s^{\,n} r_b^{\,n} \quad \textbf{(Eq. 2-18)}$$

$$R_{BB_n} = r_s^{\,n-1} r_b^{\,n} \quad \textbf{(Eq. 2-19)}$$

2.1.6 Combined Received Response

The received signal, $r(t)$, via a multipath channel can be expressed in the following equation:

$$r(t) = \sum_{i=1}^{\infty} \alpha_i x(t - \tau_i) \quad \textbf{(Eq. 2-20)}$$

where α_i and τ_i is the amplitude and propagation delay of the signal received via the i[th] path respectively and *x(t)* is the transmitted signal. Using Eq. 2-1 to Eq. 2-9, and Eq. 2-11 to Eq. 2-20,

$$\begin{aligned} y(t) &= \frac{L_A(D)x(t-t_D)}{D} + \\ &\sum_{n=1}^{\infty}\left[\begin{array}{l} \frac{L_A(SS_n)R_{SS_n}}{SS_n}x(t-t_{SS_n}) + \frac{L_A(SB_n)R_{SB_n}}{SB_n}x(t-t_{SB_n}) \\ + \frac{L_A(BS_n)R_{BS_n}}{BS_n}x(t-t_{BS_n}) + \frac{L_A(BB_n)R_{BB_n}}{BB_n}x(t-t_{BB_n}) \end{array}\right] \\ &= \frac{L_A(D)x(t)}{D} + \\ &\sum_{n=1}^{\infty}\left[\begin{array}{l} \frac{L_A(SS_n)R_{SS_n}}{SS_n}x(t-\tau_{SS_n}) + \frac{L_A(SB_n)R_{SB_n}}{SB_n}x(t-\tau_{SB_n}) \\ + \frac{L_A(BS_n)R_{BS_n}}{BS_n}x(t-\tau_{BS_n}) + \frac{L_A(BB_n)R_{BB_n}}{BB_n}x(t-\tau_{BB_n}) \end{array}\right] \end{aligned} \quad \textbf{(Eq. 2-21)}$$

The equation is modified with a change of variable $t_2=t-t_D$ for simulation purpose. Rewriting the above equation lumping the amplitude of individual path into a signal variable α_i, we have:

$$r(t) = \alpha_D x(t-t_D) + \sum_{n=1}^{\infty} \begin{bmatrix} \alpha_{SS_n} x(t-t_{SS_n}) + \alpha_{SB_n} x(t-t_{SB_n}) \\ +\alpha_{BS_n} x(t-t_{BS_n}) + \alpha_{BB_n} x(t-t_{BB_n}) \end{bmatrix} \quad \textbf{(Eq. 2-22)}$$

where $\alpha_D = \frac{L_A(D)}{D}$, $\alpha_{SS_n} = \frac{L_A(SS_n)R_{SS_n}}{SS_n}$, $\alpha_{SB_n} = \frac{L_A(SB_n)R_{SB_n}}{SB_n}$, $\alpha_{BS_n} = \frac{L_A(BS_n)R_{BS_n}}{BS_n}$ and $\alpha_{BB_n} = \frac{L_A(BB_n)R_{BB_n}}{BB_n}$.

The first term represents the amplitude of the direct path signal and subsequent terms are the amplitude of the multipath components respectively.

2.1.7 Time Varying Channel Response

Up to this point, our discussions have been on a time-invariant propagation model. However, it is well known that the shallow water channel exhibits time varying multipath fading [4-6]. Chitre [6, 14] has made several observations on short range (~50m) variations of individual signal paths. The individual signal path is observed to exhibit approximate Rayleigh fading.

To model the time variation of individual paths, the method from [7, 15] is adopted here where each amplitude of signal path is modeled as a Rayleigh random process with a median determined by α_i as described in Eq. 2-22. To model the time correlation determined by the Doppler spread W_d, the method from [14, Appendix A] is adopted.

In order to validate this model, we made channel measurements in our local waters that will be detailed in the next few sections and compared these plots with simulated ones.

2.2 Channel Measurements

2.2.1 Experimental Setup

The experiments were conducted in the coastal sea of Singapore. The transmitter was on one ship and the receiver on the other (see Figure 2-5). An omni-directional medium frequency (resonant at 18.5 kHz) projector was used to transmit the signal (with a source level of up to 180 dB re 1 μPa 1m). The receiver was a three band nested linear vertical array of nine hydrophones. In this experiment, we utilized the 18.5 kHz receiving band. For both dry ends equipment, we had a portable personal computer (PC) with a National Instrument multi-function data acquisition card. During the sea trial, the receiving ship (ship B) remained at a fixed position while the transmitting ship (ship A), moved to different locations. GPS of the ship's locations were logged in as well. The multi-channel received signal was low pass filtered at 50 kHz and then acquired at a sampling rate of 200 kHz by the receiver PC.

2.2.2 Multipath Power Delay Profile, Delay Spread and Coherence Bandwidth

Multipath power delay profiles (MPDP) of the channels were obtained by making use of broadband binary phase shift keying (BPSK) signals modulated with pseudo noise (PN) like m-sequences [35]. The symbol rate used was 4625 bps (choice of symbol rate was limited by transducer bandwidth). The carrier frequency was 18.5 kHz. This type of sequence approximately provides us with 0.43 ms of delay resolution. Computation of the MPDP was based on [36] whereas time dispersion parameters are detailed in [15]. The m-sequence length was 255 (55 milliseconds) and was generated using the primitive polynomial of degree 8, or [435] in octal representation.

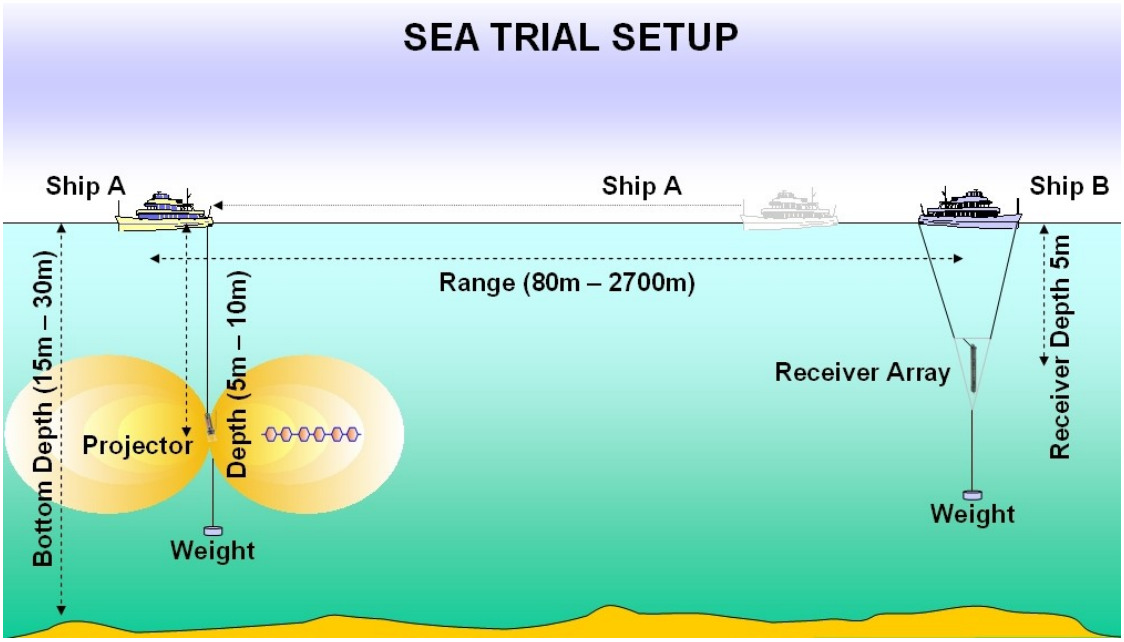

Figure 2-5. Sea trial setup

Table 2-2. Sea trial parameters

Range(m)	F_c(kHz)	F_d(ksps)	Tx Depth (m)	Rx Depth (m)	Tx Bottom Depth (m)	Rx Bottom Depth (m)
80	18.5	4625	10	5	15.6	16.5
130	18.5	4625	5	5	21.6	17.4
560	18.5	4625	10	5	15.6	16.5
1040	18.5	4625	10	5	23.0	16.5
1510	18.5	4625	10	5	26.9	16.5
1740	18.5	4625	8	5	17.2	18.9
2740	18.5	4625	10	5	26.0	18.9

Based on ray paths modelling described in Section 2.1, we deduced that PN periods of 55 ms were adequately long for multipath profiling and processing gain for all cases from 80 m to 2.7 km (see Figure 2-6). The signal was transmitted and acquired for 60 seconds for the various distances.

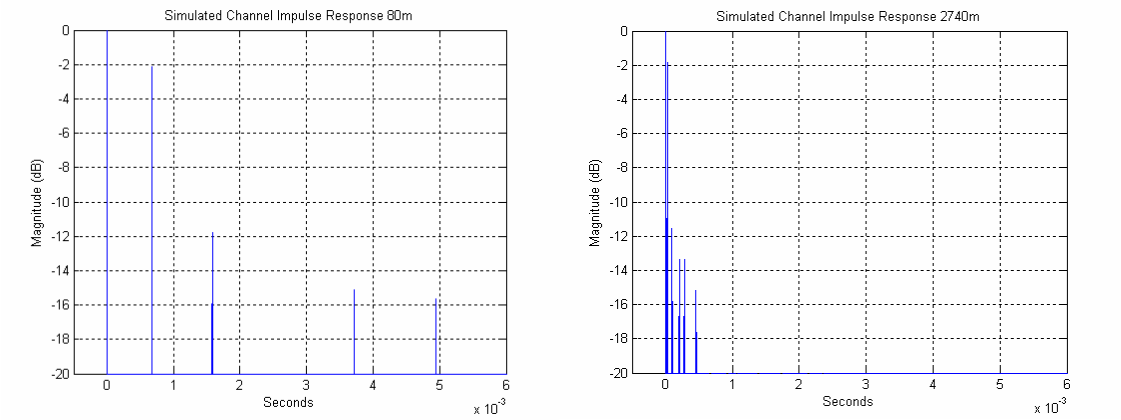

Figure 2-6. Simulated channel impulse response for 80m and 2740m respectively

The MPDP for each m-sequence frame were computed based on [36]. Each MPDP was placed next to each other over time to allow the reader to interpret the time history (y-axis) changes in multipath arrivals (in terms of delay (x-axis) and magnitude changes (intensity of z-axis)) (see Figure 2-7). It was noted that the MPDP frames were shifted in time due to transmitter and receiver motion, even though the ships were anchored (Figure 2-7). Hence, an additional step of aligning the frames was needed to align the first arrivals of all MPDP frames. The MPDP frames were re-aligned in a mean square error (MSE) fashion by comparing the first frame with the subsequent frames (Figure 2-8).

We refer to Cox [36] who used the following to compute the average power delay profile with a set of *N* envelope delay profiles,

$$P(\tau) = \frac{1}{N}\sum_{i}^{N} E_i^2(\tau) = \left\langle \left| h(\tau) \right|^2 \right\rangle_i \quad , \qquad \textbf{(Eq. 2-23)}$$

where $h(\tau)$ is the bandpass impulse response and $E_i^{\,2}(\tau)$ is the i^{th} power delay profile.

The average power delay profile can be viewed in Figure 2-9.

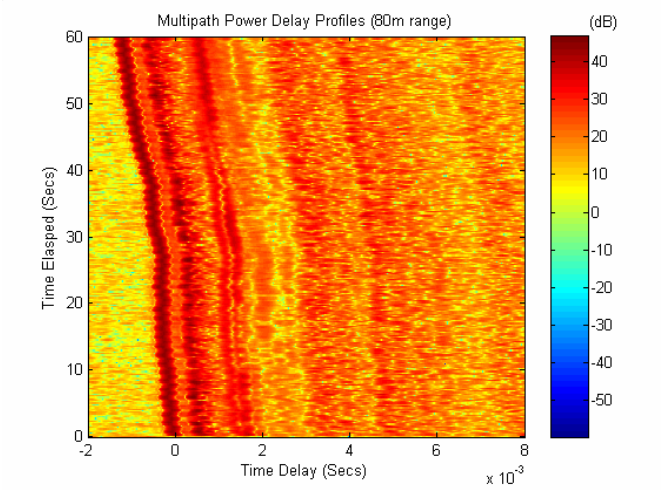

Figure 2-7. Multipath delay profiles with time shifts due to ships' motion.

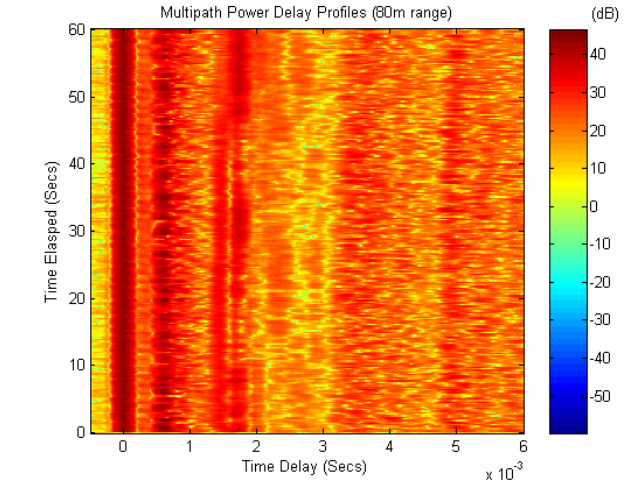

Figure 2-8. Multipath delay profiles after MSE alignment.

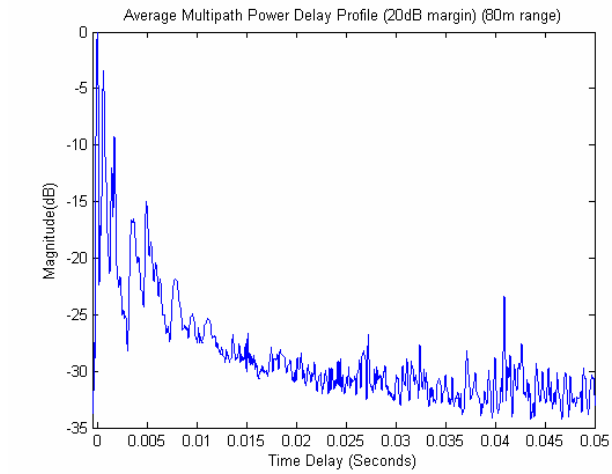

Figure 2-9. Average multipath power delay profile

Figure 2-8 shows the variation in the multipath structure. The (first) direct path did not vary too much as scattering may only be due to micropaths that were caused by small inhomogeneities in the medium and other suspended scatterers. The (second) surface reflected or the SS_1 path showed more variation and was more severely scattered due to micropaths as well as sea surface wave motion on the reflection point.

Transmission range approx 453m

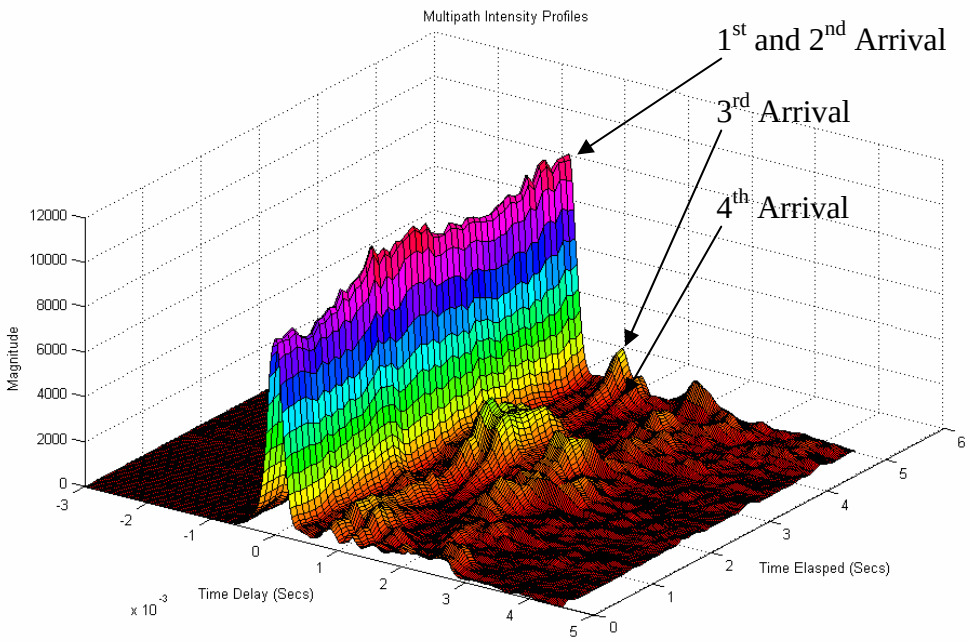

Figure 2-10. Channel impulse response - MPDPs close up plot for first five seconds

Figure 2-10 shows another way of plotting the impulse response that depicts the multipath reception at the receiver due to reflections from the physical boundaries of the channel. This test was done at a distance of 453m. As such the D and SS_1 path would probably have combined together to give a less faded first arrival component. It showed that the transmitted signal was time spread. The second characteristic derived from the time variation in the structure of the multipath. The time variations appeared to be unpredictable to the user and it was reasonable to characterize the time variant

multipath channel statistically. We also note the scattering seemed uncorrelated and the variation of magnitude of each arrival indicated some Doppler spread.

2.2.2.1 Delay Spread

Two different ways were used to quantify the delay spread. The first is the excessive delay spread $T_{m\ (20dB)}$. It is the time span whereby the multipath energy remains above a certain threshold (in this case we use 20dB) with respect to the strongest arrival. T_m is preferred in designing waveforms that are sensitive to inter symbol interference (ISI).

However, a more reliable measure of delay spread is the root mean square (rms) delay spread, σ_τ instead of T_m [15].

$$\sigma_\tau = \sqrt{\overline{\tau^2} - \left(\overline{\tau}\right)^2} \qquad \textbf{(Eq. 2-24)}$$

where

$$\overline{\tau^2} = \frac{\sum_k P(\tau_k)\tau_k^2}{\sum_k P(\tau_k)} \qquad \textbf{(Eq. 2-25)}$$

and

$$\overline{\tau} = \frac{\sum_k P(\tau_k)\tau_k}{\sum_k P(\tau_k)} \qquad \textbf{(Eq. 2-26)}$$

In practice, values of $\overline{\tau}$, $\overline{\tau^2}$, and σ_τ depend on the choice of noise threshold used to derive $P(\tau)$. The noise threshold is needed to prevent the thermal noise from being included as part of the multipath component. If the threshold is set too low, the rms delay estimated may be too high. Time dispersion parameter estimation usually requires a good noise margin. Otherwise, the estimation will be unrealistically high. Here, the threshold margin was set to be 20dB. Figure 2-11 shows the delay profiles for 80m and 2740m after flooring out the noise. The reduction of the delay spread at 2740m was expected as the range-depth ratio was larger, thereby reducing the time difference of arrivals between the direct and reflected rays.

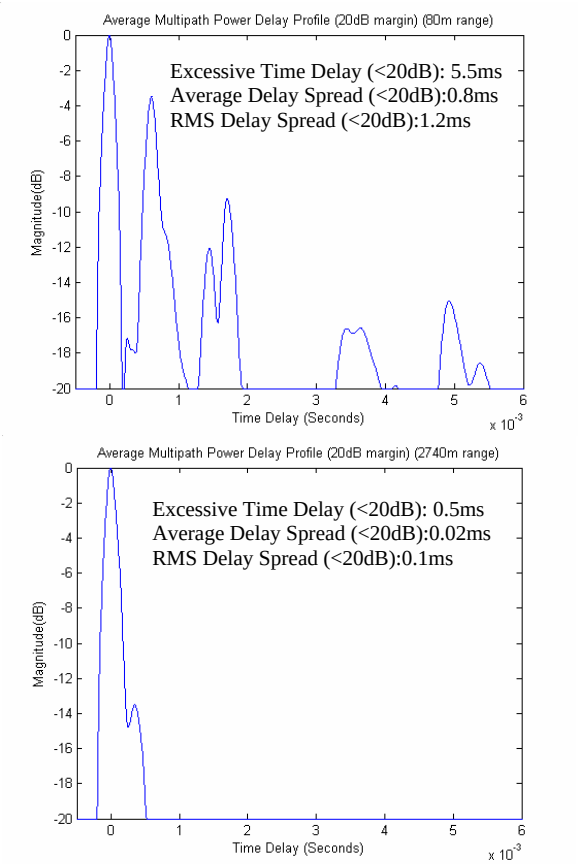

Figure 2-11. Average multipath power delay profiles (Top:80m, Bottom:2740m) after flooring at 20dB

Comparing Figure 2-6 and Figure 2-11, similarities in both figures could be noted. The simulated and actual magnitude decay of multipath arrivals was approximately the same. This means they had similar delay spreads and multipath structures.

2.2.2.2 Coherence Bandwidth

The coherence bandwidth is a statistical measure of the range of frequencies over which the channel can be considered "flat". In other words, coherence bandwidth is the frequency range where all frequency components are correlated and basically fade together. The coherence bandwidth is taken to be the reciprocal of five times the rms delay spread, σ_τ [37].

$$B_c = \frac{1}{5\sigma_\tau} \qquad \textbf{(Eq. 2-27)}$$

Note that the coherence bandwidth estimates here are "ball park estimates". Spectral analysis and simulation would be required to determine the actual impact the time varying multipath has on a particular transmitted signal.

The time averaged MPDPs were used to compute the rms delay spread, which was used to determine the coherence bandwidth using Eq.2-27. Table 2-3 summarizes the delay measurements for distances from 80m to 2740m.

Shown below is a table to summarize the delay spread and coherence bandwidth results.

Table 2-3. Delay spread and coherence bandwidth results for different ranges

Range (m)	T_m (ms) Excessive Time Delay	σ_τ (ms) RMS Time Delay	Approx Coherence Bandwidth (Hz)
80	5.5	1.2	167
130	7	1.9	105
560	3	0.85	235
1040	3.5	0.85	235
1510	2.5	0.38	526
1740	1.3	0.13	1538
2740	0.5	0.10	2000

It was noted that the delay spread generally decreases as distance increases. It's also noted that the density (over time delay) and reverberations of multipath arrivals reduces with range. Multipath and reverberations were stronger in shorter ranges.

Correspondingly, the coherence bandwidth of the channel increases with distance. Due to the 0.43ms delay resolution of the BPSK signal, the actual rms delay spread at 2.7km might be even smaller than estimated here. Unfortunately, the projector's limited bandwidth did not permit a higher delay resolution BPSK signal to be used.

From communication design perspective, we gather that if $T_m > T_s$ or $\sigma_\tau > 0.1T_s$, then the channel has frequency selective fading. These means that there is considerable ISI or inter symbol interference. One countermeasure on ISI is to adopt a rake receiver

structure. If $T_m << T_s$ or $\sigma_\tau < 0.1 T_s$ occurs in a channel, then flat fading occurs. However, the Signal to Noise Ratio (SNR) can still decrease due to destructive multipath so designs should focus on power control or diversity. Other than indicating the type of fading, T_m also determines the guard time in waveform design and if required, the length of a receiver's equalizer. Frequency domain nulls are prevalent in a multipath environment and it is more severe when the multipath arrivals are stronger (deeper nulling) and sparsely located in delay time (frequent nulling). Therefore, with shorter delay spread in time, the frequency nulls will be further apart creating a larger coherence bandwidth. The coherence bandwidth is useful when designing a modulation scheme which utilizes frequency diversity. For example, in orthogonal frequency division multiplexing (OFDM), a high data rate signal is broken into many narrowband low rate signals to counter ISI. For a narrow band signal, distortion is usually minimized if the bandwidth of the signal is less than the coherence bandwidth. Results collected tend to conclude that it is basically a **frequency selective fading** channel.

2.2.3 Doppler Effects

Conventionally, CW signals can be used to determine the Doppler effects. However, the Doppler resolution in the cross ambiguity function of CW signals is always a trade off with delay resolution (longer pulse width). Moreover, it is a narrowband signal that may not represent the total Doppler effects on our broadband communication signals. Hence, Doppler effects of the channel were captured by transmitting, acquiring and analyzing m-sequence BPSK signals. These large bandwidth-duration BPSK signals are able to provide high Doppler and delay resolution [38]. It is similar to the BPSK signals used to measure the multipath power delay profiles, but the sequence length is much longer. The m-sequence length is

16383 and is generated using primitive polynomial of degree 14, or [42103] in octal representation [35]. This type of long sequence can approximately give 0.43ms of delay resolution as well as 0.3Hz of Doppler resolution. The method for delay-Doppler computation is detailed in [38] and the functional diagram is shown in the figure below.

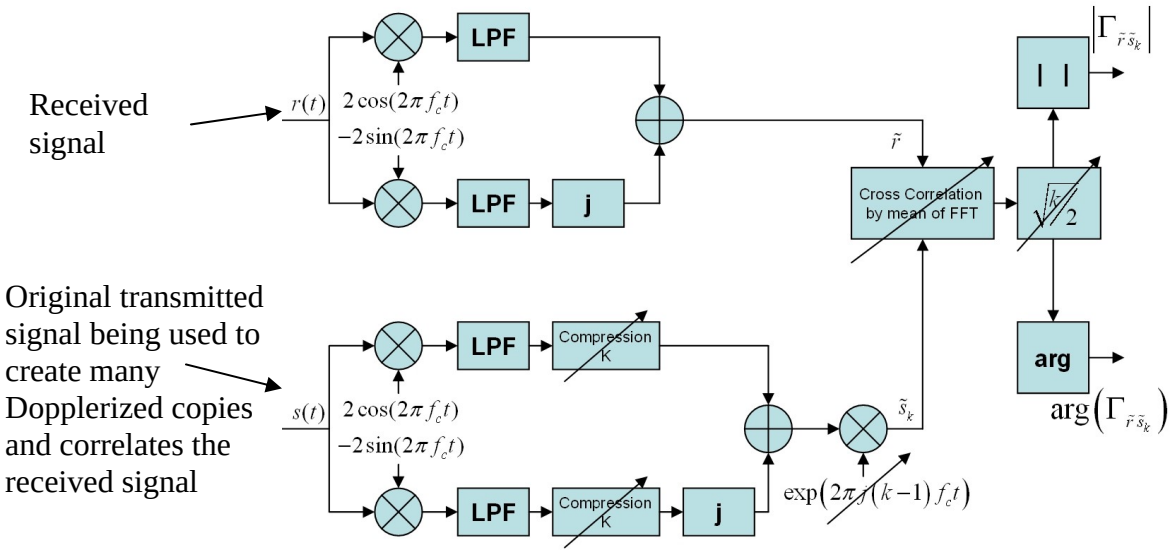

Figure 2-12. Multi-Doppler matched filter after demodulation [38]

Figure 2-12 shows the complex baseband equivalent of the received signal, *r(t)*, has been correlated with many different Dopplerized copies of the complex baseband equivalent of transmitted signal, *s(t)*. These will generate a 2-D plot of Doppler spectrum where x-axis is the time delay, y-axis is the Doppler and the z-axis shows the magnitude of the Doppler spectrum.

The challenge here was the numerical calculation of the compression time. This required either to widely oversample the signal or to interpolate it. Here, we tried the `resample()` function in MATLAB® to compress or expand the original signal and it was able to give a 1Hz resolution. The resample function uses a poly-phase filter to change the sampling rate, which in turn compresses or expands the signal in time index. Any higher Doppler resolution than 1 Hz will cause a six digit length FIR filter

to be implemented in the MATLAB® resample function and the function will hang or exit prematurely as the FIR length is too long for MATLAB® to handle. When we replaced *r(t)* with the original signal *s(t)* in Figure 2-12, we are effectively calculating its cross ambiguity function (across Doppler and time delay) at the output, $\left|\Gamma_{\tilde{r}\,\tilde{r}_s}\right|$. Figure 2-13 shows the cross ambiguity function using the numerical calculation mentioned above. Each sequence's length is increased to give better Doppler resolutions.

Figure 2-13 clearly shows that the Doppler resolution is dependent on the time duration of the BPSK modulated m-sequence. As this duration increases (from top to bottom of Figure 2-13), the Doppler resolution in the ambiguity plots start to increase too. Unlike in conventional CW methods, which time delay resolution will decrease with increased Doppler resolution, the right hand side of Figure 2-13 also shows that the time delay resolution remain the same (determine by its bit rate) even as the m-sequence length/Doppler resolution increases.

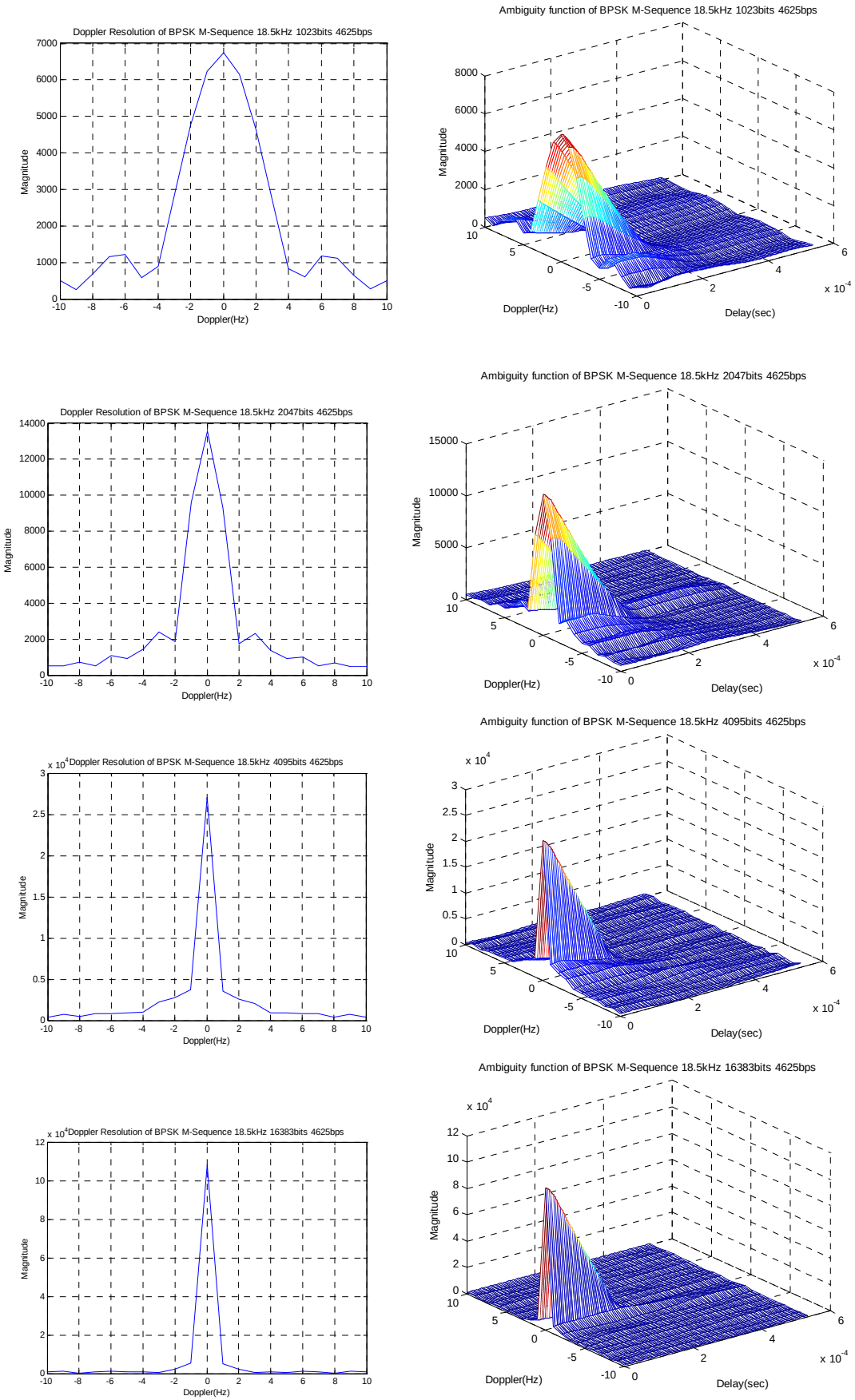

Figure 2-13. Doppler resolution/ambiguity functions of various length BPSK m-sequence

2.2.3.1 Doppler Spread

The mean frequency shift of a received signal due to relative motion between the receiver and the transmitter over some window of time is referred to as the Doppler shift, whereas the fluctuations of frequency around this Doppler shift is referred to as the Doppler spread. Doppler spread arises from variations in the height of the surface reflection point, which is caused by wind driven waves. In our case, it could also be caused by the rocking motion of the projector and hydrophones being tethered from ships. These would, in turn, cause time-variations in the direct and reflected path lengths. As a result, the signal would be phase modulated and the bandwidth of this phase modulation (via Carson's rule) will be known as the estimated Doppler spread, f_d [4]. Doppler shifts and spread indicates the time variations in the multipath structure. These Doppler effects increases with the centre frequency.

The Doppler spectrum (see Figure 2-14) will provide some form of reference for the communication designer in implementing Doppler correction algorithms. Doppler spread, f_d, is defined here as the null to null bandwidth. If ($B=1/T_s$) < f_d, then the channel develops fast fading which could lead to severe distortion, irreducible BER and synchronisation problems. If $B>f_d$, then **slow fading** (the time duration that the channel remains correlated is long compared to the transmitted symbol) occurs and the primary degradation is low SNR. No signal distortion is present. This was the case for all the channel measurements carried out and also due to the high bandwidth communication signal we employed.

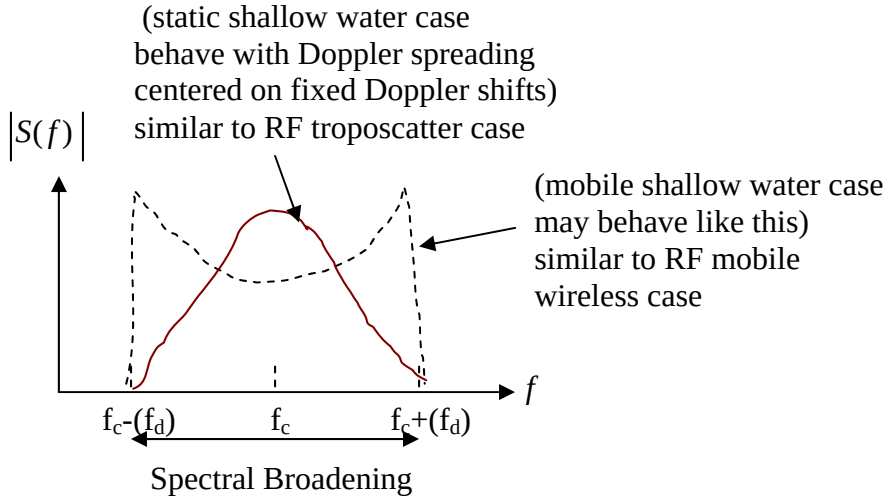

Figure 2-14. Typical Doppler spectrum

2.2.3.2 Coherence TIme

Coherence time is the expected time duration within which two signals remain correlated. Coherence time can be approximated from Doppler spread using (Eq. 2-28). A shorter coherence time will translate to a multipath structure that varies more frequently.

$$T_0 \approx \frac{0.5}{f_d} \qquad \textbf{(Eq. 2-28)}$$

Graphically we can view coherence time from the space time correlation function [37] which is derived from the scattering function *S(v)*. The space time correlation function and the Doppler power spectrum are known to be fourier transform pairs hence the inverse relationship in (Eq. 2-29)

$$\rho(\Delta t) = \int_{-\infty}^{\infty} S(v) e^{-j2\pi\Delta t v} dv \qquad \textbf{(Eq. 2-29)}$$

If $\rho(\Delta t)$ is a unit or levelled function, then the channel is time invariant. Similarly, if $T_o<T_s$, fast fading will occur and if $T_o>T_s$, then slow fading occurs.

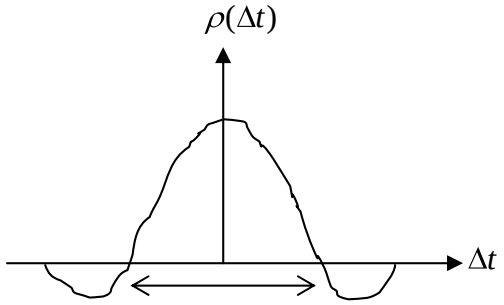

Figure 2-15. Spaced time correlation function

The delay-Doppler measurement plots at 90m and 2740m are illustrated in Figure 2-16 to Figure 2-19 to give an overview of Doppler spreading trends versus range. In Figure 2-16 and Figure 2-17, it shows the time history of Doppler effects of short range channel (80m). It could be noted that the shorter-range channels produces more Doppler spread when compared to those in Figure 2-18 and Figure 2-19. Therefore, it could be concluded that Doppler spread derived from sea surface effect (as describe in section 2.2.3.1) was more dominant at shorter ranges and these Doppler spread diminished as the range increased. From Figure 2-16 and Figure 2-18, it is noted that the Doppler effects on individual paths were different. In the MPDP analyses, it is also noted that the magnitude of multipath arrivals varies more for the shorter range channels than the longer range ones. These coincide, in principle, with the Doppler spread observations. The Doppler results for all the distances are tabulated in Table 2-4. These gave an overview of Doppler spreading trends versus distance. The Doppler shift depends on the relative velocity between the transmitting and receiving platform. In most cases, our anchored positions were stationary except for minor drifts due to tidal currents. Also, as the carrier frequency was in the kHz region, any relative ships' motion of less than 1m/s could cause Doppler shifts of a few Hz. This is due to the low propagation speed of the acoustic sound in sea water as compared to electromagnetic waves.

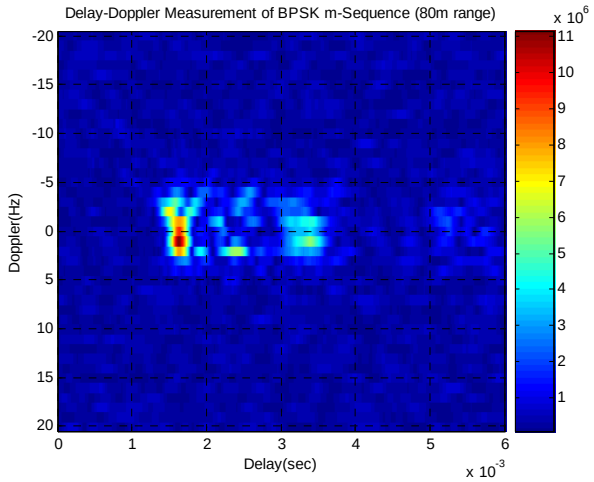

Figure 2-16. Delay Doppler measurements of BPSK m-sequence 80m

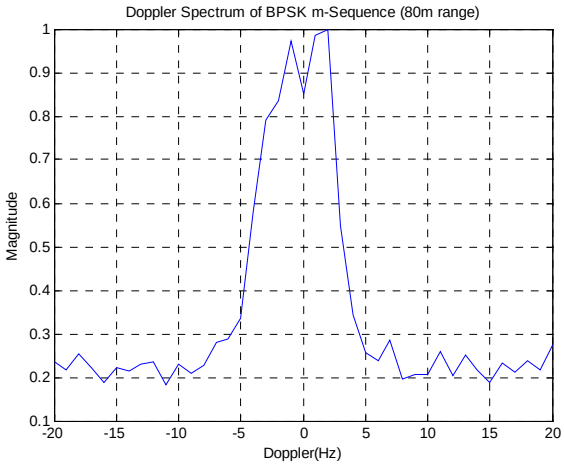

Figure 2-17 Doppler spectrum of BPSK m-sequence 80m

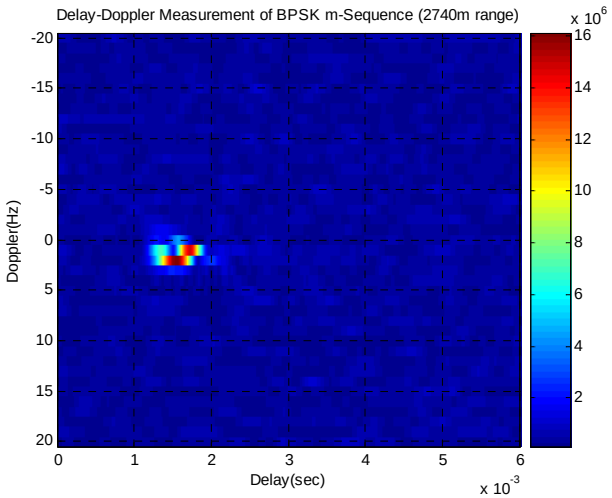

Figure 2-18. Delay Doppler measurements of BPSK m-sequence 2740m

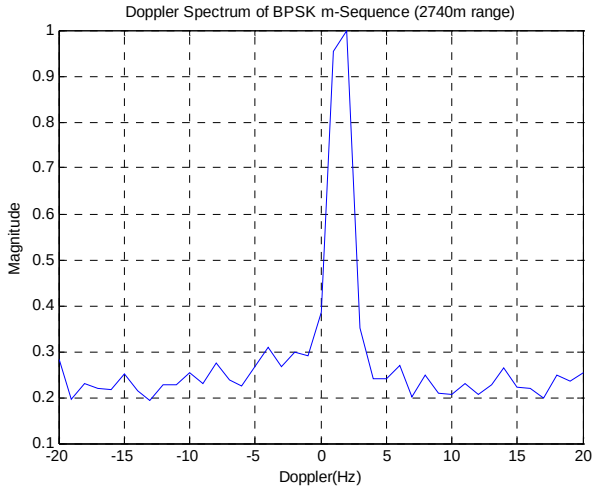

Figure 2-19. Doppler spectrum of BPSK m-Sequence 2740m

In general the maximum Doppler spread (null to null) was about 9Hz for the shortest range experiment (80m) and decreased to about 2-3 Hz for the longest range experiment (2740m). The Doppler shift was about +/-2 Hz for all the ranges. In a single carrier communication system where the bandwidth is high, the Doppler effects are very small and slow fading can be assumed. However in multi-carrier communication, if the sub-carrier bandwidth is small enough, fast fading on each sub-carrier may occur. Doppler effects are expected to increase in the mobile case and will be a function of relative velocity.

Table 2-4. Doppler and coherence time results for different ranges

Range (m)	Doppler Spread $2f_d$(Hz)	Doppler Shift (Hz)	Coherence Time (sec)
80	9	-1,+2	1/9
130	8	-1	1/8
560	4	-2	¼
1040	3	0	1/3
1510	2	-1	½
1740	2	+1	½
2740	3	+2	1/3

Our channel measurements and analysis results in Table 2-3 and Table 2-4 have shown that delay and Doppler spreads decreased at longer distances. This means

that at longer distances (up to 2.7km), the channel was capable of supporting higher bit rates. At shorter distances, techniques to mitigate ISI and Doppler may be needed in order to achieve the same level of performance as at longer distances.

2.2.4 Ambient Noise

In [9], it was noted that low frequency ambient noise in shallow Singapore waters is dominated by shipping and reclamation noise while at higher frequencies; the pre-dominant noise is snapping shrimp noise. A characteristic of snapping shrimp noise is that it is highly impulsive, resulting in a heavy tailed distribution. This implied that the Gaussian distribution, which is commonly used to characterize noise in most environments in communications, is a poor fit for the ambient noise in Singapore waters. This was backed up by data collected in [6], which also proposed the use of alpha-stable distribution to characterize the impulsiveness of snapping shrimp noise.

2.2.4.1 Stable and Gaussian Distributions

We conducted ambient noise measurements in Singapore waters over various locations at the receiver ship. The probability density function (PDF) graphs of the measured ambient noise were then plotted. By comparing them with simulated PDF plots of Gaussian and alpha-stable distributions, the best fitting distribution could be determined.

Stable distributions are a class of probability distributions that generalize the normal distribution. Alpha-stable distributions are described by four parameters. Namely the skewness parameter, the scale parameter, the location parameter and the characteristic exponent (alpha) parameter. As our noise distribution was zero-mean and symmetric, two of the parameters (skewness and location) can be set to be zero. Thus, only the remaining two parameters were estimated: the characteristic exponent (alpha) and the scale parameter, *c*, from our measurements to yield the best fit stable

distribution. These were obtained using the method described in [39]. To generate random stable variables, the methods described in [40] and [41] were used. Both the scale parameter and characteristic exponent are positive numbers, with alpha having an additional restriction: the maximum value it can take is 2. When alpha is 2, the stable distribution reduces to the familiar Gaussian distribution.

2.2.4.2 Amplitude Distribution Results

Gaussian random variables were generated using two methods: 1) by calculating the variance of the measured noise and generating Gaussian variables with similar variance, and 2) generating stable random variables as described previously, but equating alpha to 2 instead of estimating it using [41].

Our findings for one location are illustrated in Figure 2-20 and others locations have shown similar results. It shows the probability density function (PDF) of the measured noise, the estimated stable PDF and the estimated Gaussian PDFs. (See Figure 2-20)

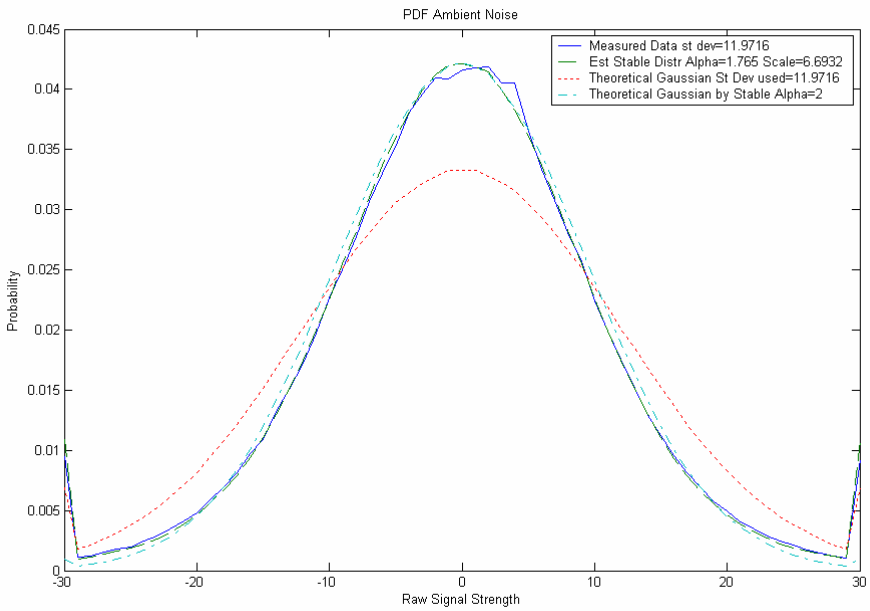

Figure 2-20. Comparison of various histograms versus measured ambient noise histogram.

The best fit alpha stable PDF had an alpha of between 1.6 and 1.8 and yields a much better fit than the Gaussian PDFs. Gaussian PDFs tend to be poor fits. As the PDFs were drawn from histogram plots, the tail ends appeared as spikes in the diagrams. These could be ignored as they simply indicated the heaviness of the tails and were not found in the actual PDFs. If the PDF of the model exhibits similar spikes as the noise PDF, it indicates good fit in the tail regions. The stable noise generator was written in MATLAB® and had been used for communication channel simulation in this work.

2.2.4.3 Noise Spectrum

Unlike deep water ambient noise, which is well defined by empirical formulas, shallow water ambient noise is subjected to wide variations. The three main sources of noise in shallow waters are shipping and industrial noise (or man-made noise), wind noise and biological noise. A power spectral density obtained from an open coastal sea of Singapore is shown in Figure 2-21. Spectral analysis of the noise also shows strong ambient noise in the low frequency (<1 kHz) regions, mainly derived from man-made shipping noise as well as surface waves. The impulsive noise will have the effect of increasing the noise floor in the spectrum. An example of impulsive noise is extracted from measurement and plotted in Figure 2-22.

For a typical noise measurement shown in Figure 2-21, the computed noise level [3] (up to 100 kHz) is 156 dB re 1 μPa 1m. And correspondingly, the spectrum noise level (up to 100 kHz): 106 dB re 1 μPa 1m. However, if only a sub-band is being used, like in a communication system, the noise level reduces to (In Band 10 kHz-26 kHz) 118 dB re 1 μPa 1m and the spectrum noise level (in Band 10 kHz - 26 kHz) is about 76 dB re 1 μPa 1m.

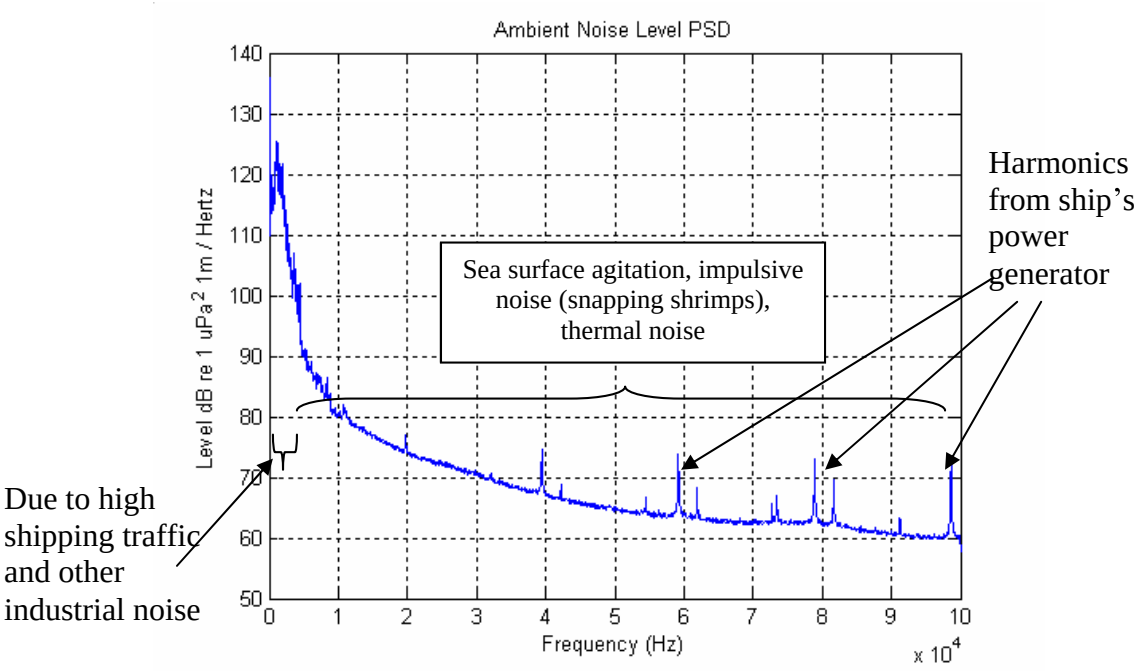

Figure 2-21. Ambient noise spectrum

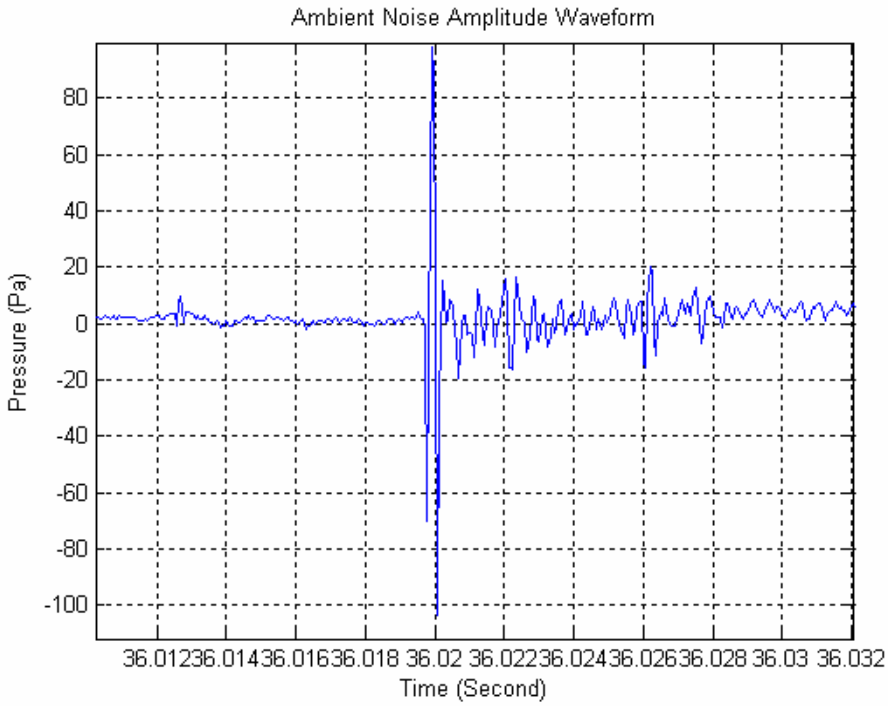

Figure 2-22. Amplitude waveform of ambient noise showing its impulsive nature (of snapping shrimp origin)

However, this does not indicate that the higher frequency band (with lower noise encountered) will experience higher Signal to Noise Ratio (SNR). The following section will shows on the SNR relationship with frequency and distance, given the local ambient noise level measured.

2.2.4.4 Range, Bandwidth and Signal to Noise Ratio (SNR)

Making use of the measured noise spectrum in the previous section, and spreading and attenuation loss assumption in Section 2.1.2 and 2.1.3 respectively, we can calculate the link budget required for a communication system. The link budget equation is expressed as [2]:

$$SNR(f,r) = SL(f) - NL(f) - L_S(r) - \frac{r}{1000} \times \beta_{dB/km}(f) \qquad \textbf{(Eq. 2-30)}$$

where

f is centre frequency in Hz
r is distance in metres
SNR is signal to noise ratio (dB)
$SL(f)$ is the source level in dB
$L_S(r)$ is the spreading loss in dB
$\beta_{dB/km}$ is the attenuation loss in dB/km
$NL(f)$ is the bandlimited noise level centred at f

For example, a Differential BPSK transmission of 190 dB re 1 μPa 1m source level is assumed and minimum SNR of 6 dB is required for a raw BER of 10^{-2} [20]. We also assume that the symbol rate is 1000 symbols per second. With that, the noise is band-limited with a 1 kHz band pass filter centred at the centre frequency to compute the noise level. The SNR for different centre frequency and distance can be calculated in MATLAB. This is illustrated in Figure 2-23 below. For distances less than 1 km, all frequencies above 10 kHz gave consistent SNRs as the attenuation loss at higher frequencies were not significant and had been compensated by the lower ambient noise in the higher band. However, as the distance increases, attenuation loss will increase and become dominant at the higher band causing the SNR to drop. For this example, it can be concluded that 12 kHz to 25 kHz band is optimum to give maximum SNR for ranges up to 4 km (See Figure 2-24).

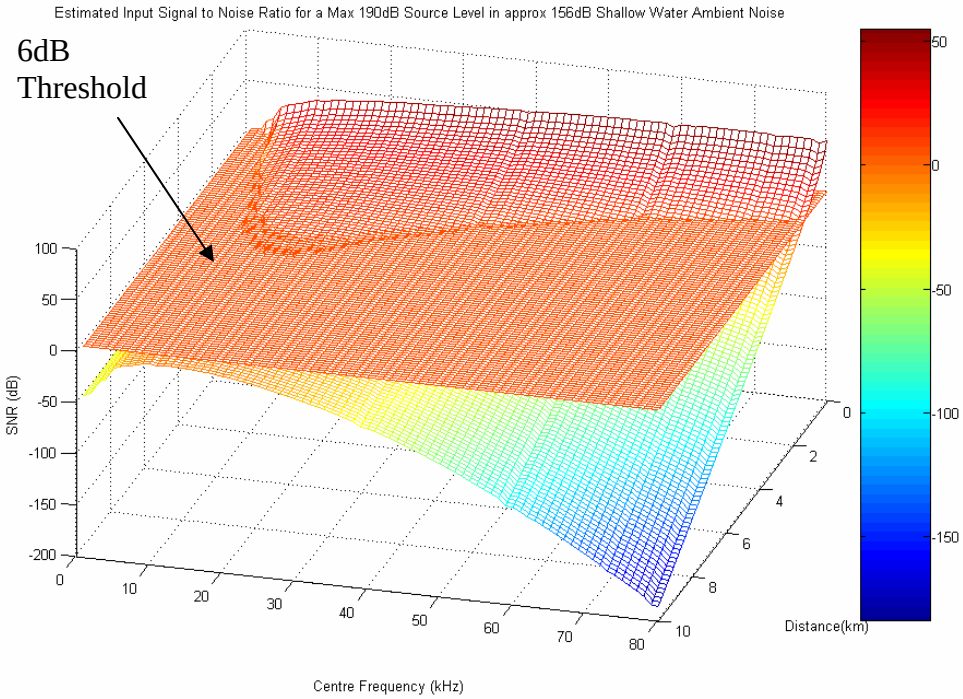

Figure 2-23. SNR performance over distance and centre frequency

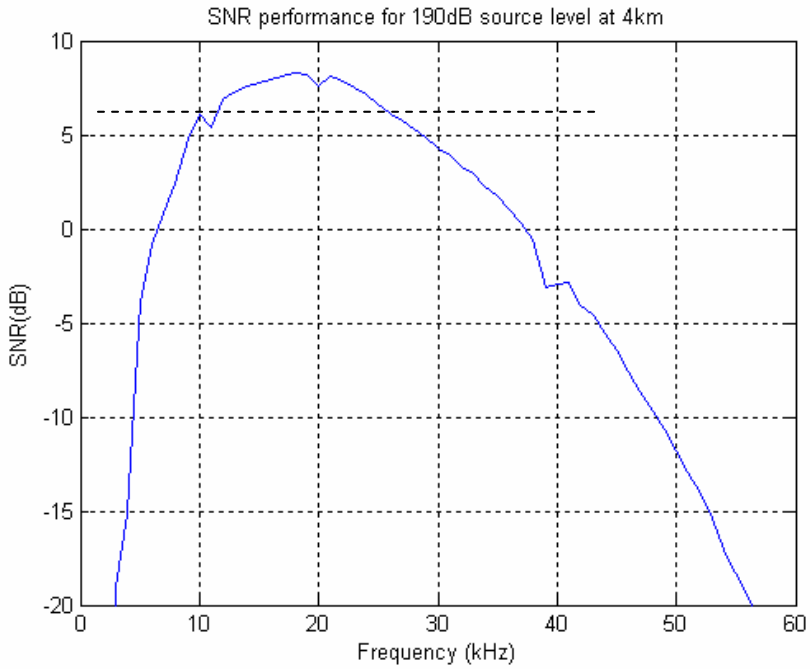

Figure 2-24. SNR performance over frequency at 4km

2.2.5 Signal Envelope Fading Characteristics

Two common stochastic channel models used to characterize a multipath fading environment are the Rayleigh and Rician models [15]. The Rician model is typically used when there is a strong line of sight (LOS) component present while the Rayleigh model assumes no such component exists.

The Rayleigh distribution [15] has a probability density function (PDF) given by

$$p(r) = \begin{cases} \frac{r}{\sigma^2}\exp\left(-\frac{r^2}{2\sigma^2}\right) & (0 \le r \le \infty) \\ 0 & (r < 0) \end{cases} \qquad \textbf{(Eq. 2-31)}$$

where r is the signal envelope, σ or sigma is the RMS value of the received voltage signal before envelope detection, and σ^2 is the time-average power of the received signal before envelope detection. The probability that the envelope of the received signal does not exceed a specified value R is given by the corresponding cumulative distribution function (CDF)

$$P(R) = P_r(r \le R) = \int_0^R p(r)dr = 1 - \exp\left(-\frac{R^2}{2\sigma^2}\right) \qquad \textbf{(Eq. 2-32)}$$

where the mean value of the Rayleigh distribution is given by

$$E[r] = \int_0^\infty rp(r)dr = \sigma\sqrt{\frac{\pi}{2}} \qquad \textbf{(Eq. 2-33)}$$

and the variance of the Rayleigh distribution is defined as σ_r^2

$$\sigma_r^2 = E\left[r^2\right] - E^2\left[r\right] = \sigma^2\left(2 - \frac{\pi}{2}\right) \qquad \textbf{(Eq. 2-34)}$$

and the median value of r is found by solving

$$\frac{1}{2} = \int_0^{r_{median}} p(r)dr \quad \Rightarrow \quad r_{median} = 1.177\sigma\,. \qquad \textbf{(Eq. 2-35)}$$

Rayleigh random variables can be generated using 2 Gaussian random variables with zero means and common variance. Varying the common variance is sufficient to generate different Rayleigh PDF plots.

The Ricean distribution is given by

$$p(r) = \begin{cases} \dfrac{r}{\sigma^2}\exp\left(-\dfrac{\left(r^2 + A^2\right)}{2\sigma^2}\right) I_0\left(\dfrac{Ar}{\sigma^2}\right) & \left(A \geq 0, r \geq 0\right) \\ 0 & \left(r < 0\right) \end{cases} \qquad \textbf{(Eq. 2-36)}$$

where the parameter *A* denotes the peak amplitude of the dominant signal and $I_0(.)$ is the modified Bessel function of the first kind and zero order. The Ricean factor, K, is also commonly used to describe the distribution and is defined as the ratio between the deterministic signal power and the variance of the multipath. It is given by $K=A^2/(2\sigma^2)$ or in terms of dB (decibels)

$$K(\text{dB}) = 10Log\left(\frac{A^2}{2\sigma^2}\right) \text{ dB} \qquad \textbf{(Eq. 2-37)}$$

Rician random variables, on the other hand, can be generated using two Gaussian random variables with non-zero means and common variance.

The best fitting Rayleigh and Rician PDFs are then determined by varying the various parameters in steps of 0.01 and calculating the corresponding mean square error (MSE). The parameters yielding the lowest MSE correspond to the best fit probability density functions (PDF)s. These PDFs and cumulative distribution functions (CDF)s are plotted out and presented in Figure 2-25 to Figure 2-28 together with their corresponding parameters and MSEs.

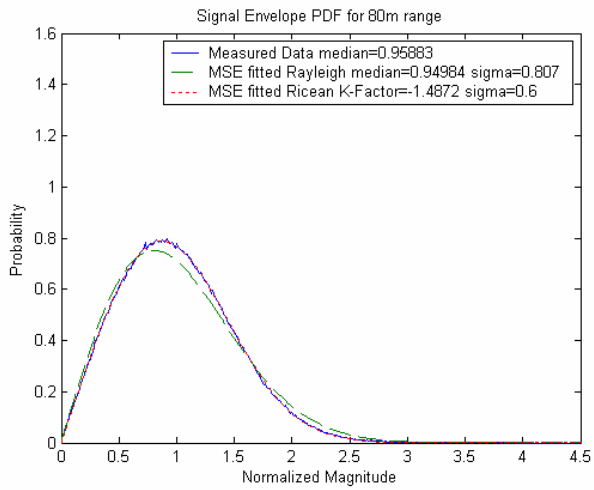

Figure 2-25. Comparative and measured PDFs for signal envelope received at 80m.

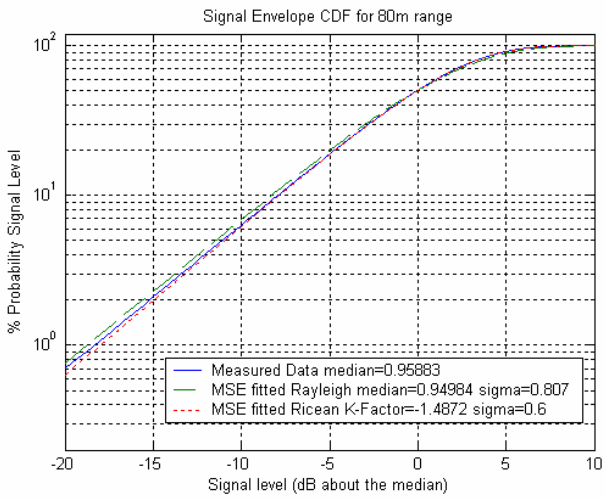

Figure 2-26. Comparative and measured CDFs for signal envelope received at 80m.

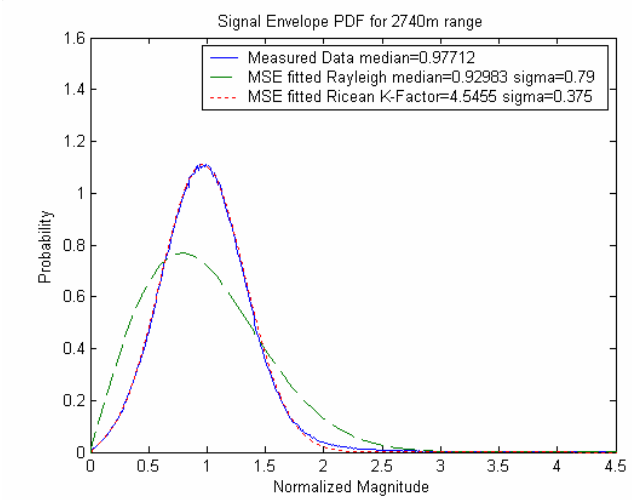

Figure 2-27. Comparative and measured PDFs for signal envelope received at 2740m

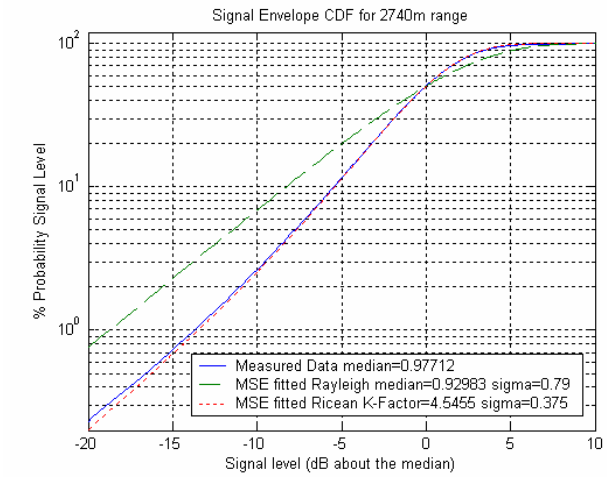

Figure 2-28. Comparative and measured PDFs for signal envelope received at 2740m

Table 2-5. Overall results for signal envelope fading for different ranges

Range (m)	MSE Fitted Rayleigh Sigma	MSE Fitted Ricean K-Factor(dB)	MSE Fitted Ricean Sigma	Approx Fit
80	0.807	-1.487	0.600	Rayleigh
130	0.803	-4.167	0.674	Rayleigh
560	0.815	2.757	0.453	Ricean
1040	0.802	-6.787	0.726	Rayleigh
1510	0.807	2.192	0.467	Ricean
1740	0.802	6.253	0.327	Ricean
2740	0.790	4.545	0.375	Ricean

These results are summarized in Table 2-5. From the table, the results indicate fading to be Rayleigh or weakly Rician at shorter distances with the exception of the 600m data set, and Rician fading at the longer ranges. Hence, less faded multipath components were more likely to be observed at the longer distances. In summary, the delay and Doppler effects are less at longer distances. Ambient noise is non-Gaussian with a heavy tailed distribution and a highly impulsive behavior. Communication system designers should exploit the channel characteristics at longer distances (>1500m up to 2740m) to transmit at higher data rates. On the other hand, it would be a serious challenge to design a modem for shorter distances that can achieve the same level of performance that was possible at longer distances.

CHAPTER 3 PRELIMINARY DPSK PERFORMANCE IN CHANNEL SIMULATOR AND SEA TRIAL

3.1 Channel Simulator

The time variant multipath channel model with alpha stable noise, described in chapter 1 and chapter 2, was implemented in MATLAB®. Figure 3-1 shows the actual multipath profile measured from a distance of 80m. Figure 3-2 shows a similar multipath profile plot for a simulated 80m distance. Hence, the channel model was able to replicate a similar multipath structure when compared to the actual channel.

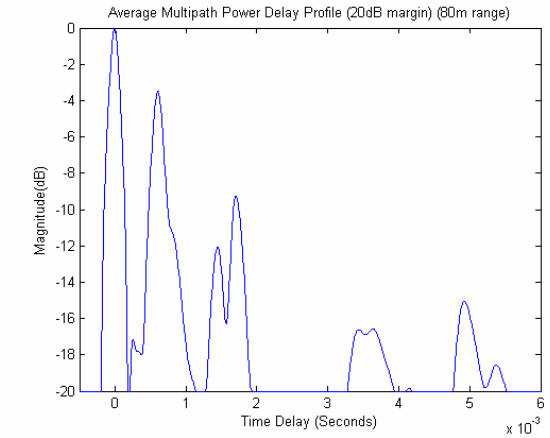

Figure 3-1. Multipath profile measurement from sea trial (80m)

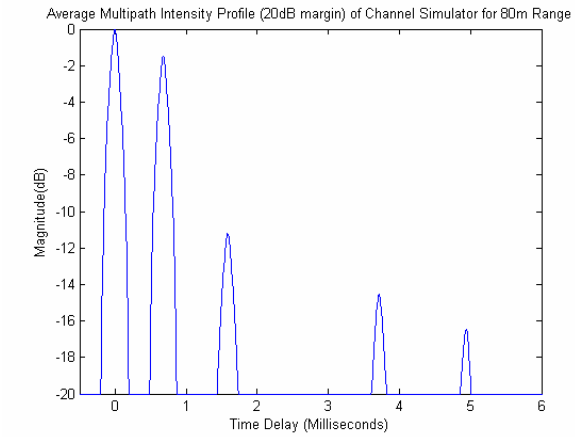

Figure 3-2. Multipath profile of channel simulator (80m)

The channel model and a Binary DPSK [20] communication system was simulated in MATLAB®. Shown in Figure 3-3 is the DBPSK frame format and other

parameters are stated in Table 3-1. A synchronisation preamble is inserted before each data frame. The preamble is a differentially encoded 128 or 512 bits m-sequence while the data segment contained 901 bits of differentially encoded pseudo random data.

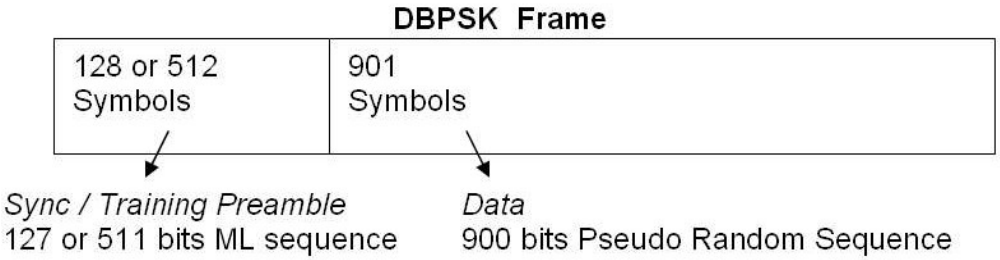

Figure 3-3. DBPSK frame format

Table 3-1. Simulation parameters

Centre Frequency	18.5kHz
Symbol Rate	9250sym/s
Raised Cosine Filter Alpha	0.25
Over sampling	16
Arbitrary Start Bit	'1'

The sync data and pseudo random data is differentially encoded as shown below.

$$d(k) = a(k)d(k-1) \qquad \textbf{(Eq. 3-1)}$$

where *d(k)* are the differentially encoded bits and $a(k) \in \{\pm 1\}$ are the original bits sequence. The arbitrary start bit is $d(0) = 1$.

The baseband antipodal DBPSK frame was raised cosine filtered, upsampled and upconverted to the band pass centre frequency at the transmitter. The signal was then fed into the channel simulator described in the previous sections. Geometrics and geophysics parameters of the channel such as transmitter's and receiver's depth, bottom depth, distance, Doppler spread, sound velocity, sea-bottom density and velocity ratios were approximates of actual sea trials. These have been presented in Chapter 2. This was done for comparison and to indicate how well the channel simulator is able to replicate the effects of shallow water channels.

At the receiver, the carrier was then removed by multiplying the signal by the sine and cosine carriers and passing the signal through a raised cosine filter. Timing recovery and synchronization is then achieved by correlating the filtered signal with the preamble sequences to obtain the best sampling instance. The data sequence was then differentially decoded (Eq.3-2) and compared with the transmitted sequence to determine the total number of errors, bit error rates (BERs) and frame error rates (FERs). The FER is the ratio of erroneous frames received to the total number of frames received.

$$\tilde{a}(k) = \mathrm{sgn}(\mathrm{Re}[r(k) \times r^*(k-1)]) \qquad \textbf{(Eq. 3-2)}$$

where *r(k)* is the complex baseband received signal after down conversion and raised cosine filtering. The simulated results are shown in Table 3-2. This will be compared with the real data analysis in the next section.

Table 3-2 Simulated BER results of binary DPSK in shallow water channels

Range (m)	SNR (dB)	No. of frames	Error bits	BER	FER
80	26.8	264	49915	2.10e-1	1
130	23.9	264	62861	2.65e-1	1
560	25.1	264	61287	2.58e-1	1
1040	20.4	198	59247	3.32e-1	1
1510	17.1	198	47448	2.66e-1	1
1740	17.5	198	3351	1.88e-2	1
2740	12.7	198	1131	6.30e-3	7.93e-1

3.2 Sea Trial

For each distance, the DBPSK frames were transmitted from ship A and received at Ship B for a duration of 60 seconds. Each DBPSK frame follows the format in Figure 3-3 and Table 3-1.

The baseband antipodal DBPSK frame was raised cosine filtered, upsampled and upconverted to the pass band centre frequency at the transmitter. This signal was

pre-prepared in MATLAB® prior to the trial. At shorter distances <1000 m, the sync preamble contained 128 bits. At longer distances, the sync preamble contained 512 bits. The reason for the change is the large magnitude variations observed in sync pulses at shorter distances and anticipated higher propagation loss at further distances. The m-sequence length was increased in-situ at longer distances to give better processing gain. Channel one at each of the ranges was selected for analysis. The signal was demodulated in the method described in the previous sub-section. The baseband data was then sampled at $T_s/2$ intervals and stored in files. T_s is the symbol interval. These were done offline in MATLAB® and the SNRs, BER and FER were computed. Table 3-4 shows the results of the analysis. The trend of decreasing BER as the distance increases, or delay spread decrease, was also observed when compared with Table 3-3 . One could also note the higher SNR at shorter ranges but the corresponding poor BERs indicate that performance degradation was largely due to strong inter-symbol interference (ISI) and higher Doppler spread measured during the trial.

Plotting the BERs of Table 3-2 and Table 3-4 into Figure 3-4, we compared the BERs of the trial and simulated data for each distance. Overall, if the BER points lie near the diagonal, it meant that the BERs of the simulated and trial data are correlated. Our simulation BERs were shown to be correlated to the BERs of the trial data. This means the channel simulator can replicate the channel encountered in sea trials. This will be further verified in the next chapter with adaptive equalization of the simulated data as well real data. If the adaptive equalizer produces the same results in terms of BERs and mean square errors, than the channel simulator is proven to be adequate close to real channel conditions.

Table 3-3. Delay spread and coherence bandwidth results for different ranges

Range (m)	Root Mean Square (RMS) Delay Spread (ms)	Doppler Spread, W_d (Hz)	Doppler Shift (Hz)
80	1.2	9	-1,+2
130	1.9	8	-1
560	0.85	4	-2
1040	0.85	3	0
1510	0.38	2	-1
1740	0.13	2	+1
2740	0.10	3	+2

Table 3-4. Trial BER results of DBPSK in shallow water channels – Channel one

Range (m)	SNR (dB)	No. of frames	Error bits	BER	FER
80	28	264	57391	2.41e-1	1
130	25.4	264	81626	3.44e-1	1
560	26.4	264	52390	2.21e-1	1
1040	20.2	198	59791	3.36e-1	1
1510	17.4	198	51465	2.89e-1	1
1740	17.4	198	2047	1.15e-2	9.90e-1
2740	12.0	198	1681	9.43e-3	9.85e-1

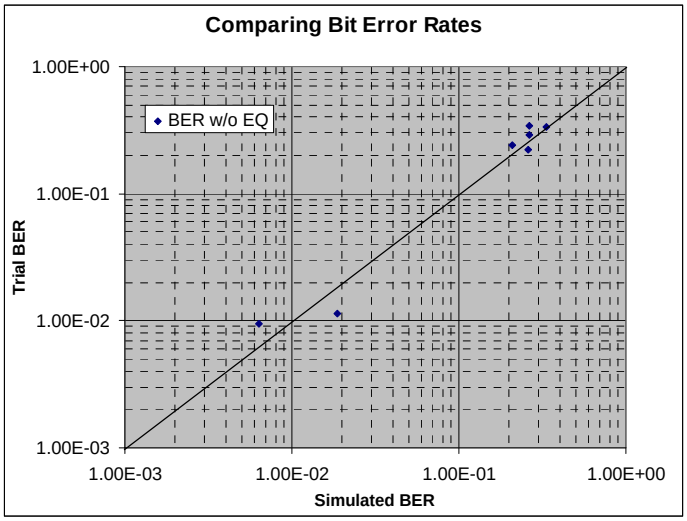

Figure 3-4. Comparing BERs of trial and simulated data for the same distance.

CHAPTER 4 ADAPTIVE EQUALIZATION, MULTICHANNEL COMBINING AND CHANNEL CODING

Shallow water channels are known for their multipaths, fading and ISI effects [8]. Without equalization or diversity techniques, achievable data rates remains very low. In order to have high data rates, adaptive equalization can be applied to compensate for the fading and ISI effects. The combinations of linear or non-linear equalization and coherent detection have been investigated extensively. However, there are comparatively fewer studies on combined equalization and non-coherent detection, although such receivers are less complex and more robust against carrier phase variation.

4.1 Linear and Decision Feedback Equalizers

Linear equalizer (LE) and Decision Feedback (DFE) [20, 42] type of equalizers have been employed in the analysis of simulated and trial data. (See Figure 4-1 and Figure 4-2).

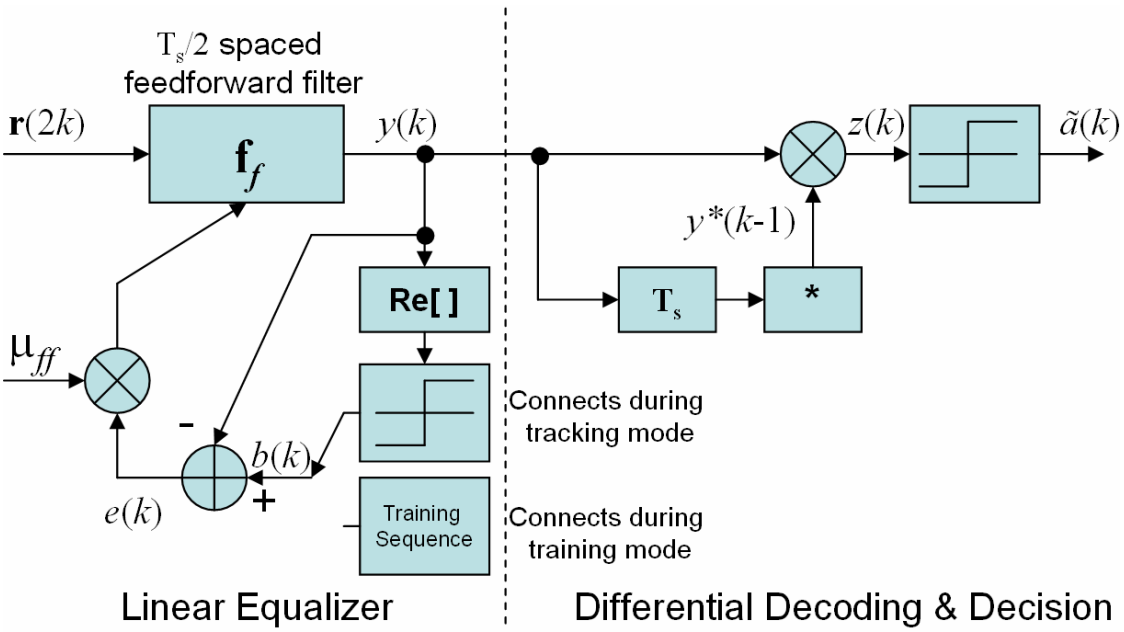

Figure 4-1. Linear equalizer

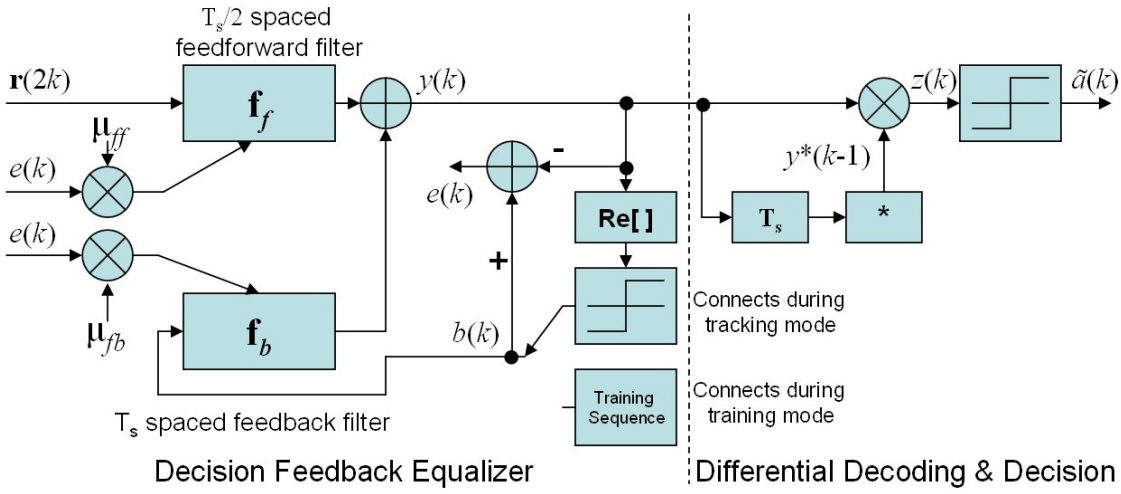

Figure 4-2. Decision feedback equalizer

Figure 4-1 shows the Linear Equalizer (LE). $y(k)$ is the output of the feedfoward filter. The taps coefficients of the feedfoward filter, $\mathbf{f}_f$, changes at every time index, k. The changes are governed by the error signal $e(k)$ and the feed forward tap adaptation step size. If the step size is too large, it may lead to instability problem. On the other hand if the step size is too small, it may lead to slow convergence rate such that the equalizer adaptation is slower than the channel rate of change. During training mode, the error signal is derived by taking the difference between the training sequence, $b(k)$, and the filter output. During tracking mode and assuming that the filter taps converges to minimize the sum squared error, the filter threshold output is assumed to be reliable enough to be used as a reference signal to compute the error signal. Figure 4-2 shows a decision feedback equalizer (DFE) and is similar to the LE except that it has a feedback filter, $\mathbf{f}_b$. A DFE can be thought of as equalizing a channel in two steps: first, a feedforward section (linear filter) shapes the overall response appropriately and attempts to make the inter symbol interference (ISI) causal, and then the feedback of sliced (quantized) outputs cancels post cursor ISI.

Note that fractionally spaced equalizers [43] were used in the analysis. The inputs to the equalizers were $T_s/2$ spaced because the signal bandwidth, after raised

cosine filtering, is about 11.5 kHz and the baud rate is 9250 symbols/seconds. In order to allow the equalizer to compensate for the distortion, sampling must be done above Nyquist rate. Thus, a $T_s/2$ sampling rate gives an effective sampling rate of 18500 sample/seconds that is adequate for 11.5 kHz wide baseband signal.

Most of the adaptive equalization for non coherent DPSK signals based their error signal between the differentially decoded soft-output and the decision output or $e(k) = \tilde{a}(k) - z(k)$ from Figure 4-1 and Figure 4-2 [44, 45]. It was noted that the error signal based on differentially decoded output may contain unnecessary higher levels of *e(k)* as a bit error in the *y(k)* will give twice the bit errors in differential decoding. This will in turn cause unnecessary filter taps adjustment even though the current detected bit in *y(k)* may be correct. On the contrary, the error signal used in this thesis was the difference between the differentially encoded training signal and the filter output, $e(k) = d(k) - y(k)$ during training, or $e(k) = \text{sgn}(\text{Re}[y(k)]) - y(k)$ during tracking.

There are mainly two sets of adaptive algorithms: one is the least mean square (LMS) and its variants and the other is recursive least square (RLS) and its variants [20-22]. A strong advantage of RLS algorithm is it converges much faster than the LMS algorithm. On the other hand, RLS algorithm has a higher complexity than the LMS. The total computational complexity of LMS algorithm has 2N+1 multiplications and 2N additions/subtraction while the RLS algorithm has a total of $4N^2$ multiplications and $3N^2$ additions/subtractions [21]. N is the total number of filter taps. Note that these requirements will double for a complex number, as in base band, implementation. Hence, we chose both LMS and RLS algorithm for our analysis in the next few sections and compared their performances. The summaries of the LMS algorithm [21] for LE and DFE were available in Table 4-1 and Table 4-2.

The number of filter taps was largely determined by the excessive delay spread. In Table 2-3, the longest excessive delay spread is 7 ms. Based on $T_s/2$ spaced equalizer, it would at least take 129 taps (from $0.007*2/T_s$) for the equalizer to be effective at 130 m range. In fact, the number of equalizer taps ought to be larger perhaps several times the length of the longest delay spread multiplied by $2/T_s$ [43]. However, increasing the number of taps further would also increase the noise in the filter as well as decreasing the convergence rate. As such, the number of feed forward taps was fixed at 129 for all distances. For LMS algorithm, the adaptation step size is usually fixed by the eigen values spread of the correlation matrix on the filter input signal and the number of the filter taps. However, the eigen values spread may change for different range-depth ratio channels. For example, a frequency selective fading channel with small range-depth ratio will have many frequency nulling in the frequency power spectrum. These nulling may have reduce the maximum values in the received signal power spectral density. As the eigen values of the correlation matrix are bounded by the minimum and maximum values of the power spectral density [21], the eigen value spread may be small. Instead of computing different optimum step size for different ranges and data sets, a fixed step size was chosen for all ranges for simplicity. The feed forward step size was found optimum at 0.04 by trial and error. Similarly the step size for the feedback filter was set at 0.004. The adaptation step size will be reduced four times after training as the reference signal for taps adaptation during the tracking phase is no longer reliable. This method has seen improved tracking performance where the MSSE remains levelled and does not increase during tracking phase. In the RLS algorithm, the forgetting factor was chosen to be 0.99 [23]. By trial and error, the RLS algorithm will only work in a short range of forgetting factor settings ~ typically 0.98 to 0.999 and it has to be less than one for

stability and convergence [21]. The setting of the kronecker delta in the RLS algorithm is not important as its effect diminishes exponentially the k^{th} iteration increases. The delta value was arbitrary set to two. Like the LMS algorithm, the RLS algorithm filter adaptation had been deliberately reduced to 30% during the tracking phase. This value was found to increase the equalizer performance at all distances.

Table 4-1. Summary of LE-LMS algorithm

Input:	$\mathbf{f}_f$(k) Feed forward filter tap coefficient vector of size N $\mathbf{r}$(2k) Input vector of size N at $2/T_s$ sampling rate *b(k)* Training signal / tracking signal μ_{ff} Feed forward tap adaptation step size (0.04) N – No. of feed forward filter taps (129) k^{th} iteration
Output:	*y(k)* Filter output at T_s sampling rate $\mathbf{f}_f$(k+1) Feed forward tap coefficient vector update

1. Filtering:

$$\mathbf{r}(2k) = \left[r(2k+\tfrac{N-1}{2})\ r(2k+\tfrac{N-2}{2})\ ...r(2k)...\ r(2k-\tfrac{N-2}{2})\ r(2k-\tfrac{N-1}{2}) \right]^{\mathrm{T}} \quad \textbf{(Eq. 4-1)}$$

$$\mathbf{f}_f(k) = \left[f_{f_0}\ f_{f_1}\ .....f_{f_{N-1}} \right]^{\mathrm{T}} \quad \textbf{(Eq. 4-2)}$$

$$y(k) = \mathbf{f}_f(k)^{\mathrm{T}} \times \mathbf{r}(2k) \quad \textbf{(Eq. 4-3)}$$

2.Reference Signal:

During training $\Rightarrow b(k) = d(k)$ **(Eq. 4-4)**

During tracking $\Rightarrow b(k) = \mathrm{sgn}(\mathrm{Re}[y(k)])$ **(Eq. 4-5)**

3.Error Estimation:

$$e(k) = b(k) - y(k) \quad \textbf{(Eq. 4-6)}$$

4.Tap Coefficient Adaptation:

During training $\Rightarrow \mathbf{f}_f(k+1) = \mathbf{f}_f(k) + \mu_{ff} e(k) \mathbf{r}^*(k)$ **(Eq. 4-7)**

During tracking $\Rightarrow \mathbf{f}_f(k+1) = \mathbf{f}_f(k) + \dfrac{\mu_{ff}}{4} e(k) \mathbf{r}^*(k)$ **(Eq. 4-8)**

Table 4-2. Summary of DFE-LMS algorithm

Input: $\mathbf{f}_f$(k) Feed forward filter tap coefficient vector of size N_f
$\mathbf{f}_b$(k) Feed back filter tap coefficient vector of size N_b
$\mathbf{r}$(2k) Input vector of size N_f at $2/T_s$ sampling rate
$\mathbf{b}$(k) Feed back vector of size N_b at T_s sampling rate
b(k) Training signal / Tracking signal
μ_{ff} Feed forward tap adaptation step size (0.04)
μ_{fb} Feed back tap adaptation step size (0.004)
N_f – No of feed forward filter taps (65)
N_b – No of feed back filter taps (64)
k^{th} iteration

Output: *y(k)* Filter output at T_s sampling rate
$\mathbf{f}_f$(k+1) Feed forward tap coefficient vector update
$\mathbf{f}_b$(k+1) Feed back tap coefficient vector update

1. Filtering:

$$\mathbf{r}(2k) = \left[r(2k+N-1)\ r(2k+N-2)\ ...r(2k) \right]^{\mathrm{T}} \quad \textbf{(Eq. 4-9)}$$

$$\mathbf{f}_f(k) = \left[f_{f_0}\ f_{f_1}\ .....f_{f_{N_f-1}} \right]^{\mathrm{T}} \quad \textbf{(Eq. 4-10)}$$

$$\mathbf{b}(k) = \left[b(k-1)\ b(k-2)\ ...b(k-N_b) \right]^{\mathrm{T}} \quad \textbf{(Eq. 4-11)}$$

$$\mathbf{f}_b(k) = \left[f_{b_0}\ f_{b_1}\ .....f_{b_{N_b-1}} \right]^{\mathrm{T}} \quad \textbf{(Eq. 4-12)}$$

$$y(k) = \left(\mathbf{f}_f(k)^{\mathrm{T}} \times \mathbf{r}(2k) \right) + \left(\mathbf{f}_b(k)^{\mathrm{T}} \times \mathbf{b}(k) \right) \quad \textbf{(Eq. 4-13)}$$

2.Reference Signal:

During training $\Rightarrow b(k) = d(k)$ **(Eq. 4-14)**

During tracking $\Rightarrow b(k) = \mathrm{sgn}(\mathrm{Re}\left[y(k) \right])$ **(Eq. 4-15)**

3.Error Estimation:

$$e(k) = b(k) - y(k) \quad \textbf{(Eq. 4-16)}$$

4.Tap Coefficient Adaptation:

During training $\Rightarrow$ $\mathbf{f}_f(k+1) = \mathbf{f}_f(k) + \mu_{ff} e(k) \mathbf{r}^*(k)$ **(Eq. 4-17)**

$$\mathbf{f}_b(k+1) = \mathbf{f}_b(k) + \mu_{fb} e(k) \mathbf{b}^*(k) \quad \textbf{(Eq. 4-18)}$$

During tracking $\Rightarrow$ $\mathbf{f}_f(k+1) = \mathbf{f}_f(k) + \frac{\mu_{ff}}{4} e(k) \mathbf{r}^*(k)$ **(Eq. 4-19)**

$$\mathbf{f}_b(k+1) = \mathbf{f}_b(k) + \frac{\mu_{fb}}{2} e(k) \mathbf{b}^*(k) \quad \textbf{(Eq. 4-20)}$$

Summaries of RLS algorithm [21] for LE and DFE are detailed in Table 4-3 and Table 4-4.

Table 4-3. Summary of LE-RLS algorithm

Input:	$\mathbf{f}_f$(k) Feed forward filter tap coefficient vector of size N $\mathbf{r}$(2k) Input vector of size N at $2/T_s$ sampling rate *b(k)* Training signal / tracking signal δ Value to initialize $\mathbf{\Phi}^{-1}(0)$ (2) λ Forgetting Factor (0.99) N – No. of feed forward filter taps (129) k^{th} iteration $\mathbf{\Phi}^{-1}(0) = \delta\mathbf{I}$ where **I** is the N by N size identity matrix
Output:	*y(k)* Filter output at T_s sampling rate $\mathbf{f}_f$(k+1) Feed forward tap coefficient vector update

1. Filtering:

$$\mathbf{r}(2k) = \left[r(2k+\tfrac{N-1}{2})\ r(2k+\tfrac{N-2}{2})\ ...r(2k)...\ r(2k-\tfrac{N-2}{2})\ r(2k-\tfrac{N-1}{2}) \right]^{\mathrm{T}} \quad \textbf{(Eq. 4-21)}$$

$$\mathbf{f}_f(k) = \left[f_{f_0}\ f_{f_1}\ .....f_{f_{N-1}} \right]^{\mathrm{T}} \quad \textbf{(Eq. 4-22)}$$

$$y(k) = \mathbf{f}_f(k)^{\mathrm{T}} \times \mathbf{r}(2k) \quad \textbf{(Eq. 4-23)}$$

2.Reference Signal:

During training $\Rightarrow b(k) = d(k)$ **(Eq. 4-24)**

During tracking $\Rightarrow b(k) = \mathrm{sgn}(\mathrm{Re}\left[y(k)\right])$ **(Eq. 4-25)**

3.Error Estimation:

$$e(k) = b(k) - y(k) \quad \textbf{(Eq. 4-26)}$$

4.Tap Coefficient Adaptation:

$$\mathbf{u}(k) = \mathbf{\Phi}^{-1}(k-1) \times \mathbf{r}^{*}(2k) \quad \textbf{(Eq. 4-27)}$$

$$\mathbf{g}(k) = \frac{\mathbf{u}(k)}{\lambda + \mathbf{r}(2k)^{\mathrm{T}}\mathbf{u}(k)} \quad \textbf{(Eq. 4-28)}$$

$$\mathbf{\Phi}^{-1}(k) = \frac{1}{\lambda}\left(\mathbf{\Phi}^{-1}(k-1) - \left(\mathbf{g}(k)\mathbf{r}(2k)^{\mathrm{T}}\mathbf{\Phi}^{-1}(k-1)\right)\right) \quad \textbf{(Eq. 4-29)}$$

During training $\Rightarrow \mathbf{f}_f(k+1) = \mathbf{f}_f(k) + e(k)\mathbf{g}(k)$ **(Eq. 4-30)**

During tracking $\Rightarrow \mathbf{f}_f(k+1) = \mathbf{f}_f(k) + 0.3e(k)\mathbf{g}(k)$ **(Eq. 4-31)**

Table 4-4. Summary of DFE-RLS algorithm

Input:	$\mathbf{f}_f$(k) Feed forward filter tap coefficient vector of size N_f $\mathbf{f}_b$(k) Feed back filter tap coefficient vector of size N_b $\mathbf{r}$(2k) Input vector of size N_f at $2/T_s$ sampling rate $\mathbf{b}$(k) Feed back vector of size N_b at T_s sampling rate *b(k)* Training signal / Tracking signal δ Value to initialize $\mathbf{\Phi}^{-1}(0)$ (2) λ Forgetting Factor (0.99) N_f – No of feed forward filter taps (65) N_b – No of feed back filter taps (64) k^{th} iteration
Output:	*y(k)* Filter output at T_s sampling rate $\mathbf{f}_f$(k+1) Feed forward tap coefficient vector update $\mathbf{f}_b$(k+1) Feed back tap coefficient vector update

1. Filtering:

$$\mathbf{r}(2k) = \left[r(2k+N-1)\ r(2k+N-2)\ ...r(2k)\right]^{\mathrm{T}} \quad \textbf{(Eq. 4-32)}$$

$$\mathbf{f}_f(k) = \left[\ f_{f_0}\ f_{f_1}\ .....f_{f_{N_f-1}}\ \right]^{\mathrm{T}} \quad \textbf{(Eq. 4-33)}$$

$$\mathbf{b}(k) = \left[b(k-1)\ b(k-2)\ ...b(k-N_b)\right]^{\mathrm{T}} \quad \textbf{(Eq. 4-34)}$$

$$\mathbf{f}_b(k) = \left[\ f_{b_0}\ f_{b_1}\ .....f_{b_{N_b-1}}\ \right]^{\mathrm{T}} \quad \textbf{(Eq. 4-35)}$$

$$\mathbf{a}(k) = \begin{bmatrix} \mathbf{r}(2k) \\ \mathbf{b}(k) \end{bmatrix} \quad \textbf{(Eq. 4-36)}$$

$$\mathbf{f}(k) = \begin{bmatrix} \mathbf{f}_f(k) \\ \mathbf{f}_b(k) \end{bmatrix} \quad \textbf{(Eq. 4-37)}$$

$$y(k) = \left(\mathbf{f}(k)^{\mathrm{T}} \times \mathbf{a}(k)\right) \quad \textbf{(Eq. 4-38)}$$

2.Reference Signal:

During training $\Rightarrow b(k) = d(k)$ **(Eq. 4-39)**

During tracking $\Rightarrow b(k) = \mathrm{sgn}(\mathrm{Re}\left[y(k)\right])$ **(Eq. 4-40)**

3.Error Estimation:

$$e(k) = b(k) - y(k) \quad \textbf{(Eq. 4-41)}$$

4.Tap Coefficient Adaptation:

$$\mathbf{u}(k) = \mathbf{\Phi}^{-1}(k-1) \times \mathbf{a}^{*}(k) \quad \textbf{(Eq. 4-42)}$$

$$\mathbf{g}(k) = \frac{\mathbf{u}(k)}{\lambda + \mathbf{r}(2k)^{\mathrm{T}}\mathbf{u}(k)} \quad \textbf{(Eq. 4-43)}$$

$$\mathbf{\Phi}^{-1}(k) = \frac{1}{\lambda}\left(\mathbf{\Phi}^{-1}(k-1) - \left(\mathbf{g}(k)\mathbf{r}(2k)^{\mathrm{T}}\mathbf{\Phi}^{-1}(k-1)\right)\right) \quad \textbf{(Eq. 4-44)}$$

During training $\Rightarrow$ $\mathbf{f}(k+1) = \mathbf{f}(k) + e(k)\mathbf{a}^{*}(k)$ **(Eq. 4-45)**

During tracking $\Rightarrow$ $\mathbf{f}(k+1) = \mathbf{f}(k) + 0.3e(k)\mathbf{a}^{*}(k)$ **(Eq. 4-46)**

4.2 LE-LMS Performance in Simulation

The simulated data set that was analysed in Table 3-2 was used to assess the LE-LMS performance. The results were tabulated in Table 4-5. All the BERs have been reduced due to equalization when compared to Table 3-2.

Table 4-5. Simulated BER results of DBPSK in shallow water channels after LE-LMS

Range (m)	SNR (dB)	No. of frames	Error bits	BER	FER
80	26.8	264	19688	8.29e-2	1
130	23.9	264	29361	1.24e-1	1
560	25.1	264	15262	6.42e-2	1
1040	20.4	198	5305	2.98e-2	9.90e-1
1510	17.1	198	5488	3.08e-2	9.19e-1
1740	17.5	198	468	2.63e-3	5.96e-1
2740	12.7	198	1326	7.44e-3	7.88e-1

The ensemble average mean square error (MSE) of *e(k)* over all the frames at 1040 m are calculated and shown in Figure 4-3(a). It shows the equalizer has converged to its minimum mean squared error (MMSE). Figure 4-3(b) shows the tap weight adaptation results showing the estimated impulse response of the inversed channel for one of the frames. Figure 4-3(c) shows the differential decoding results if no processing was done on the input signal *r(k).* Red crosses indicate the known data bit of '0' and green circles indicate known data bit of '1'. Improvements are seen in the in-phase quadrature (IQ) plot (Figure 4-3(d)) after linear equalization.

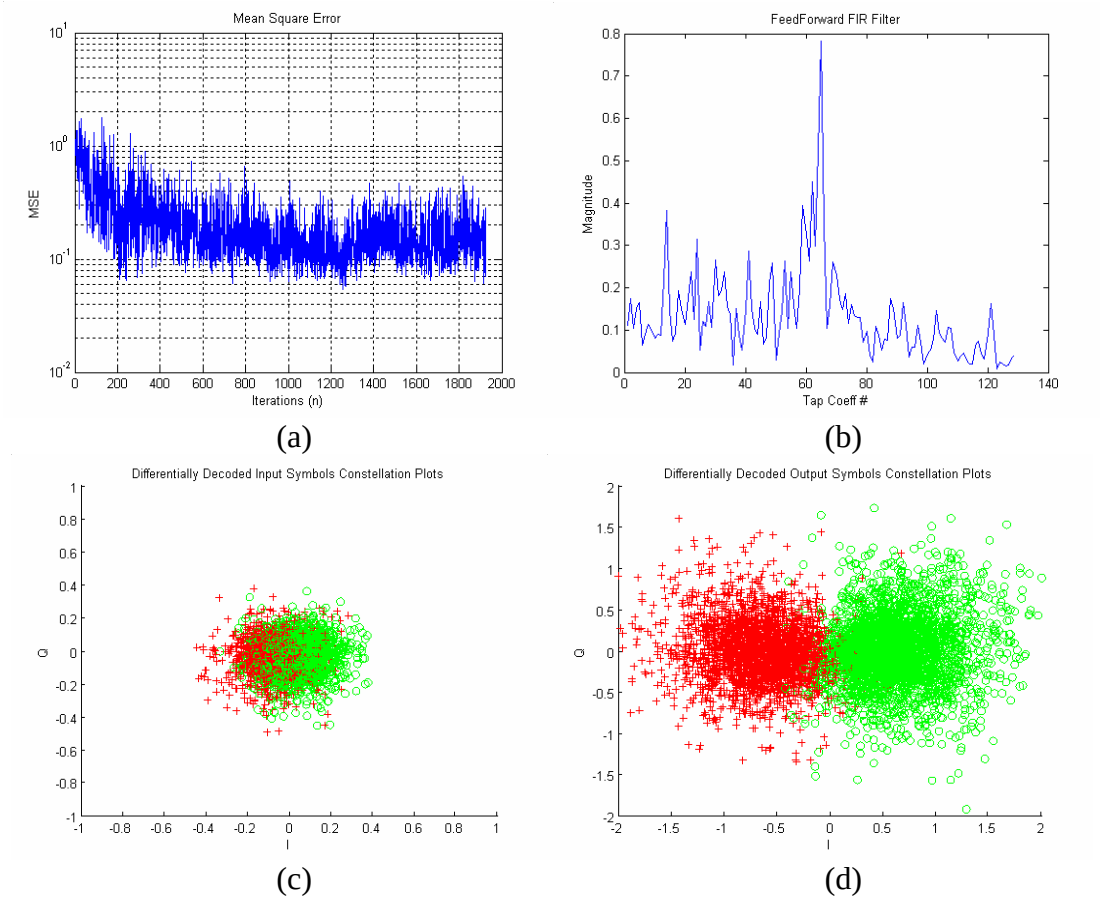

Figure 4-3. Simulated LE-LMS equalization-distance: 1040m (a) Mean square error (b) Filter tap coefficients (c)Input I-Q plot of differential decoded *r(k)* (d) Output I-Q plot of $\tilde{a}(k)$

4.3 LE-LMS Performance in Sea Trial

Similarly, the LE-LMS was applied onto the trial data to compare it with the simulated ones. And the results are shown below. Both their BERs in Table 4-5 and Table 4-6 are plotted in Figure 4-4. The 'pink' data set are which adaptive equalization were used to compensate for the ISI and to improve the BER performance

Table 4-6. Trial BER results of DBPSK in shallow water channels after LE–LMS, Channel one

Range (m)	SNR (dB)	No. of frames	Error bits	BER	FER
80	28	264	37647	1.58e-1	1
130	25.4	264	43316	1.82e-1	1
560	26.4	264	14457	6.04e-2	1
1040	20.2	198	6024	3.38e-2	1
1510	17.4	198	17561	9.85e-2	1
1740	17.4	198	542	3.04e-3	6.46e-1
2740	12.0	198	955	5.36e-3	8.39e-1

Figure 4-4 shows that their equalizer output BER results for the simulated and real case were approximately correlated. From Table 4-5 and Table 4-6, both witness the same trends of decreasing BER with increasing distance. All these also agree with the delay spread results in the channel measurements of [17].

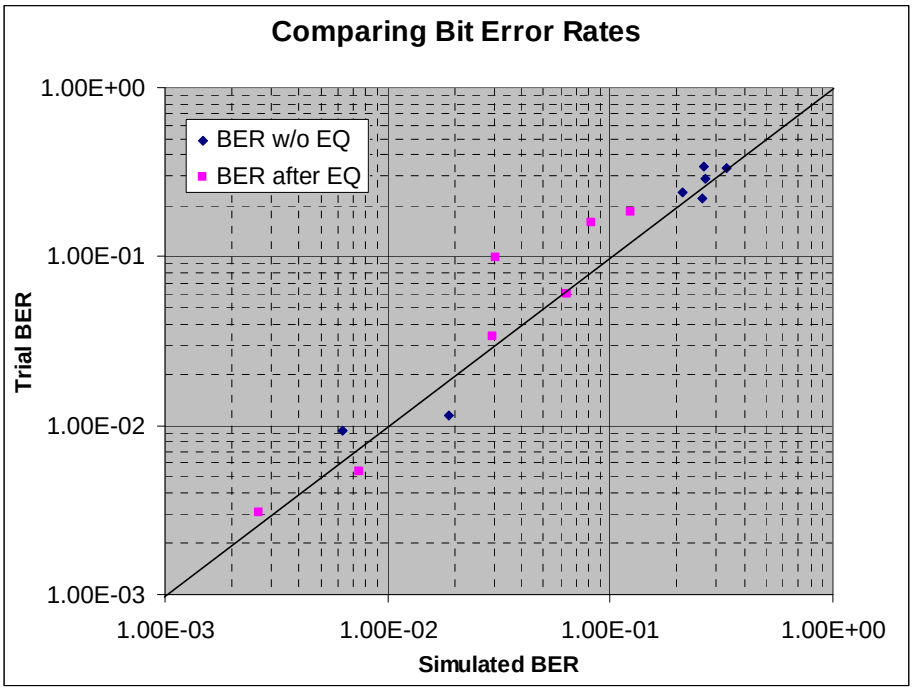

Figure 4-4 Comparing BERs of trial and simulated data for the same distance after equalization

The mean squared error, tap weights and IQ plots for the trial 1040m data set are plotted in Figure 4-5. Note the similarities in the plots when compared to Figure 4-3. Figure 4-5(a) does converge the same way as Figure 4-3(a). In addition, both their lower bounds which indicate its MMSE were also approximately the same. It can be noted too that the MMSE reduces as distance increases. The difference in plots of Figure 4-3(b) and Figure 4-5(b) is normal as the estimates for each frame will be different due fading.

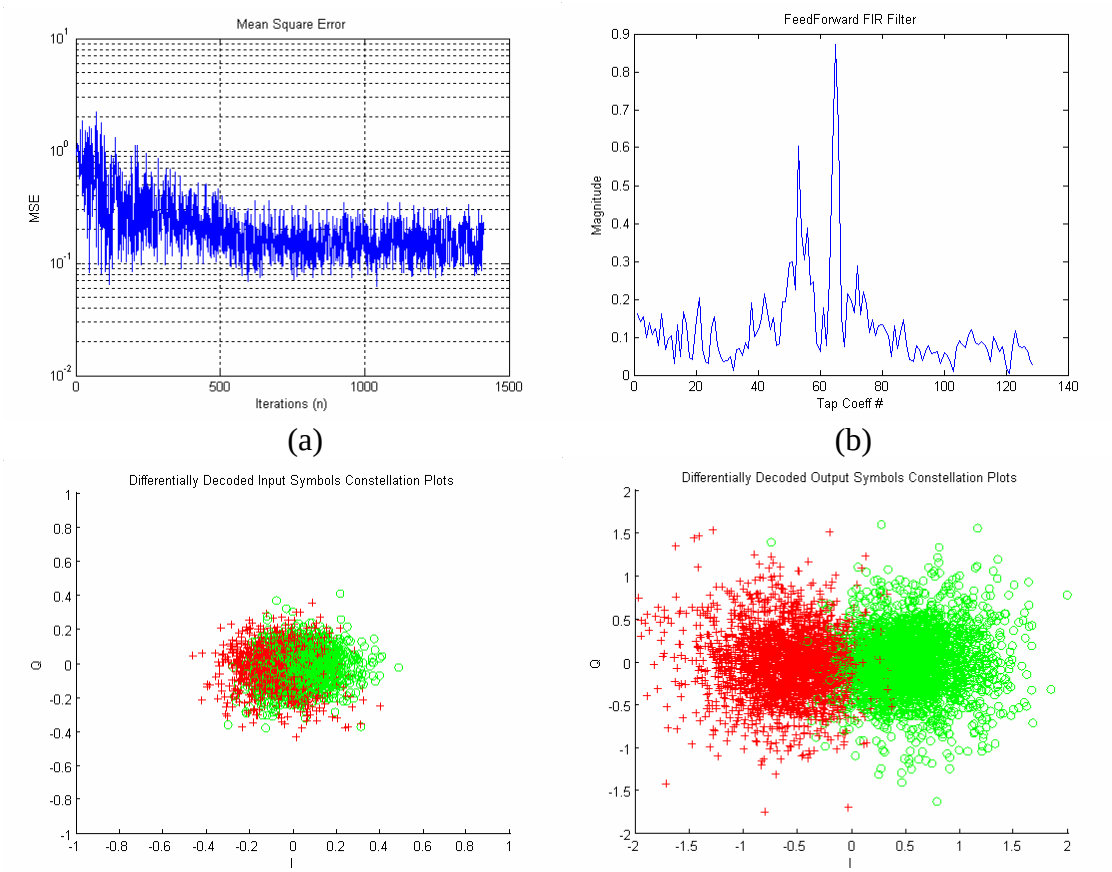

Figure 4-5. LE-LMS equalization on trial data-distance: 1040m (a) Mean square error (b) Filter tap coefficients (c) Input I-Q plot of differential decoded *r(k)* (d) Output I-Q plot of $\tilde{a}(k)$

Figure 4-3 to Figure 4-5 had shown that the channel simulator is a good approximation of the actual trial channel. The focus of this thesis at this juncture will shift its attention to improving the performance of real data. It will begin with

analysing the trial performance of DFE-LMS and compare them with the LE-LMS ones to determine which is better.

4.4 DFE-LMS Performance in Sea Trial

Similarly, DFE-LMS was applied onto the trial data, and the results were shown below in Table 4-7.

Table 4-7. Trial BER results of DBPSK in shallow water channels after DFE–LMS, Channel one

Range (m)	SNR (dB)	No. of frames	Error bits	BER	FER
80	28	264	54051	2.27e-1	1
130	25.4	264	67754	2.85e-1	1
560	26.4	264	37531	1.58e-1	1
1040	20.2	198	12929	7.26e-2	1
1510	17.4	198	18250	1.02e-1	1
1740	17.4	198	188	1.06e-3	4.24e-1
2740	12.0	198	881	4.94e-3	8.79e-1

In general the BERs for distances less than 1500m of the DFE-LMS performed poorer than the LE-LMS (see Figure 4-14). These were due to the poor input BERs for distances less than 1500m that resulted in more detected bits errors to propagate down the feedback filter, giving rise to higher mismatch in channel inversion. On the other hand, if the BER improves as in 1700-2700m, the bit errors in the feedback filter decreases resulting in better estimate to counter post ISI effects. Then the advantage of DFE kicks into effect by reducing noise feedback and feedback more accurate bit energy. This noise feedback is inherent in LE as post samples (bit energy and noise) remained in the causal part of the filter to equalize the present sample. Evidently, this could be seen in Table 4-6 and Table 4-7 or Figure 4-8 where the DFE BER performance was better than that of LE at longer distances. However, an equalizer that could perform reasonably well at all distances was preferred and the LE-LMS was chosen over the DFE-LMS to further enhance the BER performance. In the next

segment, multichannel combining with LE-LMS was introduced to further reduce the BERs.

4.5 A Note on Sparse DFE-LMS Performance in Sea Trial

A short introduction on sparse equalization had been given in chapter one. This section would explore sparse equalization to reduce noise in the estimate of the inversed channel, so as to improve the performance of the adaptive equalizer. When the adaptive channel equalizer converged, the z-transform of filter taps, *f(k)*, is proportional to *1/H(z)* where *H(z)* is the z-transform of the channel [21]. However, the most simple and robust implementation adaptive filters were usually finite impulse response (FIR) based. As the channel was significantly sparse, it was probable to deactivate the insignificant taps in *H(z)* of the equalizer to reduce noise especially in the case where the length of the filter was long. However, instead of obtaining the denominator *H(z)* from the FIR filter taps, an infinite impulse response (IIR) adaptive equalizer with a feedforward (anti-causal part) and feedback (causal part) filter was used [22, p.666-671]. With this implementation, the *H(z)* taps were directly obtainable from the feedback filter. It is also realized that the IIR filter presented in [21, p.323-329] was similar to DFE-LMS equalizer and the differences lies mainly in the feedback. The DFE feedback hard decided values while the IIR adaptive filter feedback soft values. The DFE-LMS is also fractionally spaced and involves complex numbers while the IIR in [21, 22] is *T*-spaced and involves real numbers. Since the DFE was similar to IIR equalizer, insignificant taps of the feedback taps, where its value was less than 10% of the maximum feedback tap value, were deactivated in the modified DFE-LMS equalizer. This was done to find out if this will reduce the BER further.

Table 4-8 Trial BER results of DBPSK in shallow water channels after Sparse DFE–LMS, Channel one

Range (m)	SNR (dB)	No. of frames	Error bits	BER	FER
80	28	264	47360	1.99e-1	1
130	25.4	264	58123	2.47e-1	1
560	26.4	264	32399	1.36e-1	1
1040	20.2	198	18544	1.04e-1	1
1510	17.4	198	22612	1.26e-1	1
1740	17.4	198	226	1.27e-3	4.44e-1
2740	12.0	198	1035	5.80-3	9.39e-1

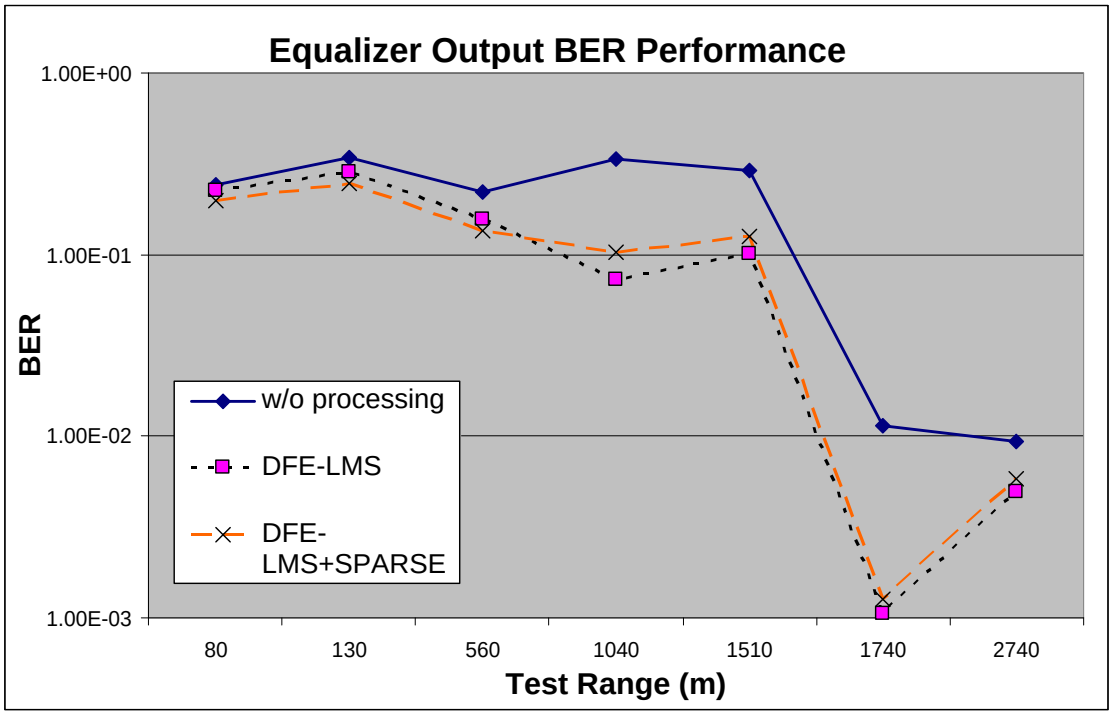

Figure 4-6 Comparing DFE-LMS and sparse DFE-LMS performance

Result for the sparse DFE-LMS was slightly better than DFE-LMS for the shorter three distances and slightly worse than the DFE-LMS alone for other distances. The slight improvement might be due to the presence of sparse arrivals in the channel response (see Figure 2-11) while there was less sparse arrival in the longer distances. It could also mean that transducer bandwidth has limited the sparse channel effect in the receiver and closely packed arrivals are smeared. As the improvement was not significant, other methods of improvement would be assessed.

4.6 LE-RLS Performance in Sea Trial

In addition to the LMS algorithm, the RLS algorithm would be used on the trial data. The purpose was to find out if the performance improvement obtain from RLS was necessary for reliable communication. As such, the thesis will pick the best performing equalizer from the LMS and RLS algorithms. Multichannel combining and channel coding will then be applied to both equalizers to check its final performance. If the LMS algorithm suffice reliable communication (>90% packets retrieved from all distances), then it will be desired to implement this as the complexity is much lower. On the other hand, the RLS algorithm is expected to work better than the LMS as it is faster in convergence but higher in complexity. The LE-RLS combination was applied to the sea trial data, and the results were shown below in Table 4-9.

Table 4-9. Trial BER results of DBPSK in shallow water channels after LE–RLS, Channel one

Range (m)	SNR (dB)	No. of frames	Error bits	BER	FER
80	28	264	17863	7.52e-2	1
130	25.4	264	22056	9.28e-2	1
560	26.4	264	1828	7.69e-3	9.32e-1
1040	20.2	198	2920	1.64e-2	9.90e-1
1510	17.4	198	12506	7.02e-2	1
1740	17.4	198	252	1.41e-3	4.54e-1
2740	12.0	198	889	4.99e-3	8.99e-1

Again, the LE-RLS's MSE and constellation plots of 1040m were selected in Figure 4-7 for comparison with LE-LMS plots found in Figure 4-5. From the MSE plots, it could be noticed that the RLS is much faster in convergence and the noise in the MSE plot in the RLS case was also noticeably lower. This would reflect in the number of bit errors of the LE-RLS 1040m and it was 4.5 times lower than the LE-LMS 1040m case.

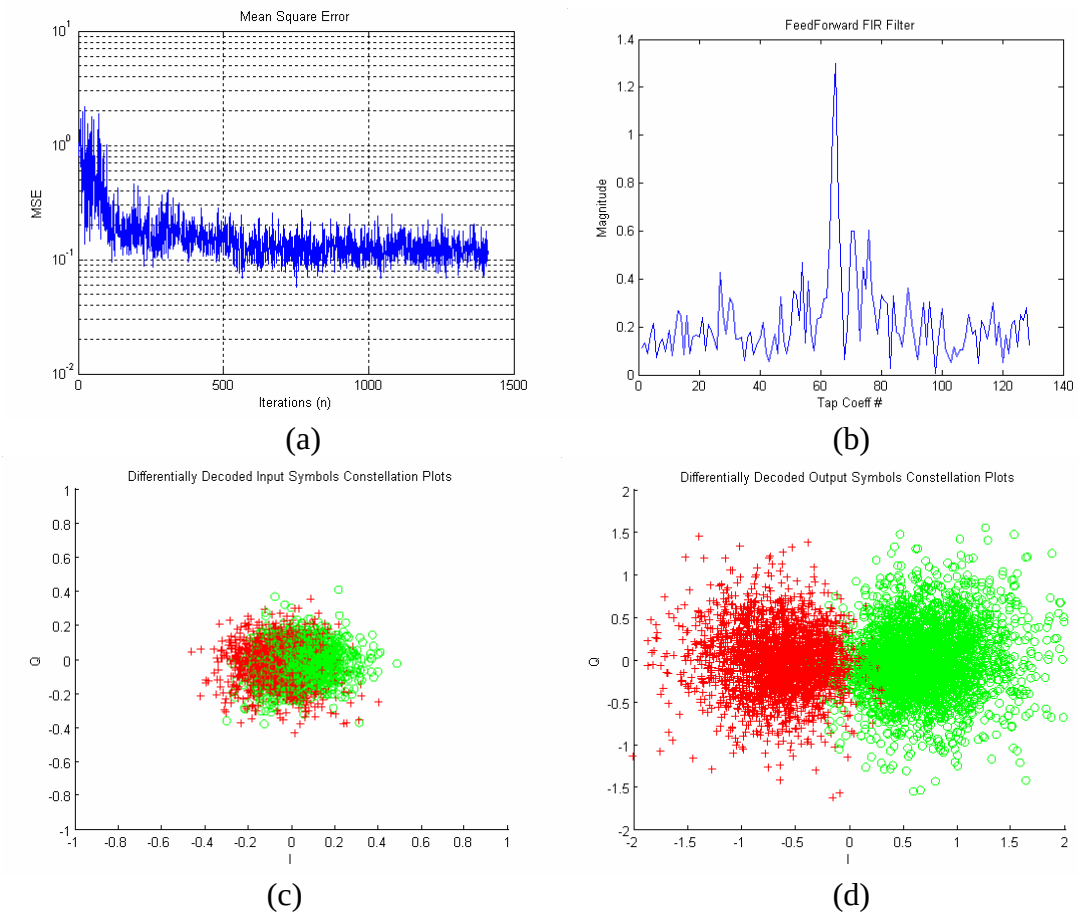

Figure 4-7. LE-RLS equalization on trial data-distance: 1040m (a) Mean square error (b) Filter tap coefficients (c) Input I-Q plot of differential decoded *r(k)* (d) Output I-Q plot of $\tilde{a}(k)$

4.7 DFE-RLS Performance in Sea Trial

Similarly, DFE-LMS was applied onto the trial data, and the results are shown below in Table 4-10. As expected the DFE-RLS perform poorer than the LE-RLS case except in the case where the input BER is low enough (1740 m, 2740 m), the DFE performed slightly better than the LE in both LMS and RLS cases.

Table 4-10. Trial BER results of DBPSK in shallow water channels after DFE–RLS, Channel one

Range (m)	SNR (dB)	No. of frames	Error bits	BER	FER
80	28	264	39946	1.68e-1	1
130	25.4	264	33076	1.39e-1	9.96e-1
560	26.4	264	4240	1.78e-2	8.67e-1
1040	20.2	198	5582	3.13e-2	8.94e-1
1510	17.4	198	17994	1.01e-1	1
1740	17.4	198	109	6.12e-4	2.73e-1
2740	12.0	198	771	4.33e-3	8.79e-1

4.8 Performance Comparison for DFE, LE, LMS and RLS

In this section, a comparison of the equalizers' BER performance was done (see Figure 4-8). In practice, if the percentage of bits in error is less than one percent, they can be successfully removed by error coding. However, based on the plot in Figure 4-8, none of the candidates are suitable for error coding evaluation. On another note, both DFEs work better than the LEs for the two furthest distances. The best performing equalizer is the LE-RLS equalizer with the lowest BER for most of the distances. The LE-RLS equalizer will be chosen for further processing, namely multichannel combining and error decoding. However, the RLS's computational complexity is rather high when compared to that of LMS, and it is desired to select a LMS equalizer for further processing. This is to make a comparison later if the multichannel combining and error decoding can improve the BER performance of a LMS based equalizer to a reliable level. Hence, the LE-LMS equalizer will also be chosen for this purpose.

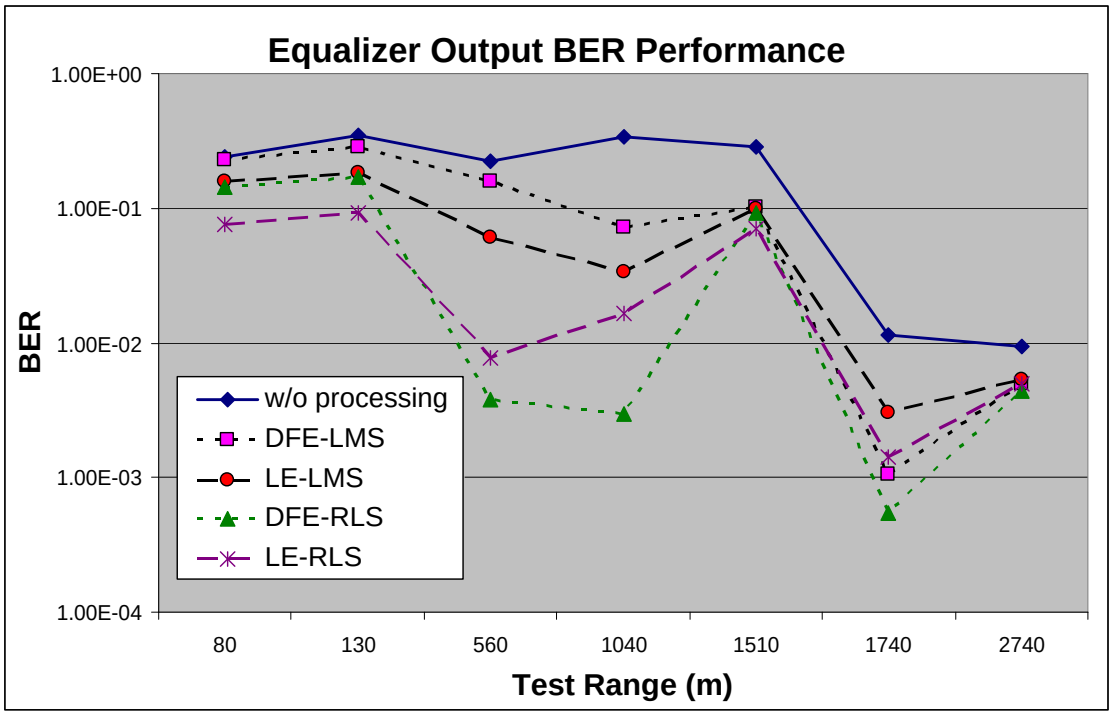

Figure 4-8 BER performance of Equalizers: LE-LMS, DFE-LMS, LE-RLS and DFE-RLS

4.9 Multichannel Combining

From the previous sections, adaptive equalization has shown their effectiveness in compensating for the distortions introduced by the multipath channel. However, these techniques gave poorer results when there are fading effects due to channel variations. A way to reduce the effect of fading is spatial diversity [25]. It is also noted that the SNR performance usually reach nominal value after the number of combined channels reaches five or more [24]. As such, all five channels ($\mathbf{r}_1(2k)$ to $\mathbf{r}_5(2k)$) sampled at $T_s/2$ in the nested array were individually synchronized, LE by LMS or RLS, then combined by summation, averaged and differentially decoded as shown in Figure 4-9 and their BER results are tabulated in Table 4-11 and Table 4-12. It shows BER reductions at all distances (see Figure 4-11).

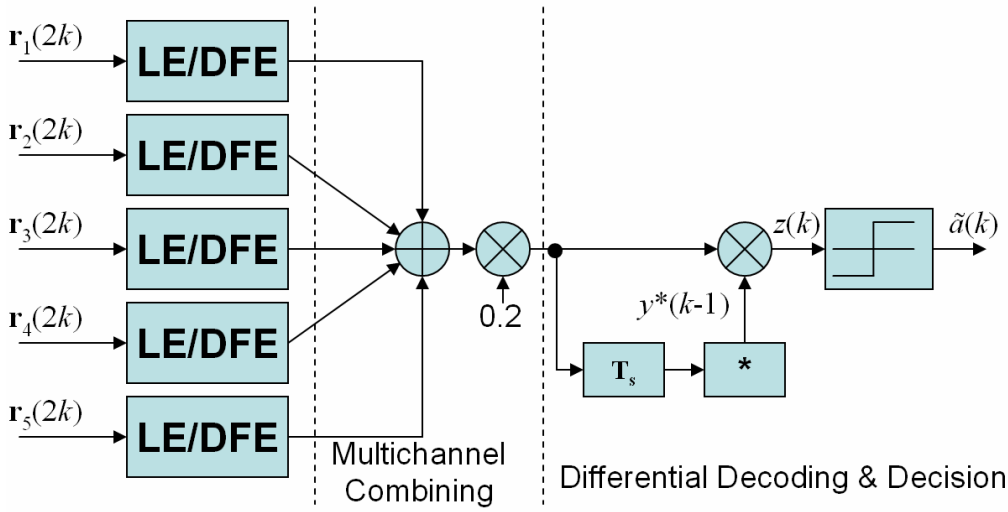

Figure 4-9. Multichannel combining method with LE or DFE

Figure 4-10 shows the effect of multichannel combining in decreasing the BER. This was also evident by comparing the IQ plots Figure 4-10(d) and Figure 4-10(e). At all distances, the bit errors, BERs and FERs had been reduced (see Figure 4-11 and Figure 4-12). The BER performance gain from multichannel combining seemed to be higher at the shorter distances than in the longer distances. At the shorter ranges, the received signal had high SNR but there was a lot of multipath. Multichannel combining effectively does beamforming as each channel is synchronized to the strongest arrival [23]. At shorter distances, as the distinct multipath arrivals' angles were largely different, they were separable by beamforming. Hence, by suppressing the unwanted interfering multipaths, the BER performance would improve. In the case of the longer distances, the differences in the angle of multipath arrivals were going to be smaller than the array beamwidth, so it was inseparable by the five element array. The only form of gain from multichannel combining will be the gain in SNR. As it is noted that the input SNRs at the longer distances are rather low (see Table 4-10), the increased in SNR after multichannel combining had helped to reduce the BERs. The next segment will show the channel coding performance of trial data.

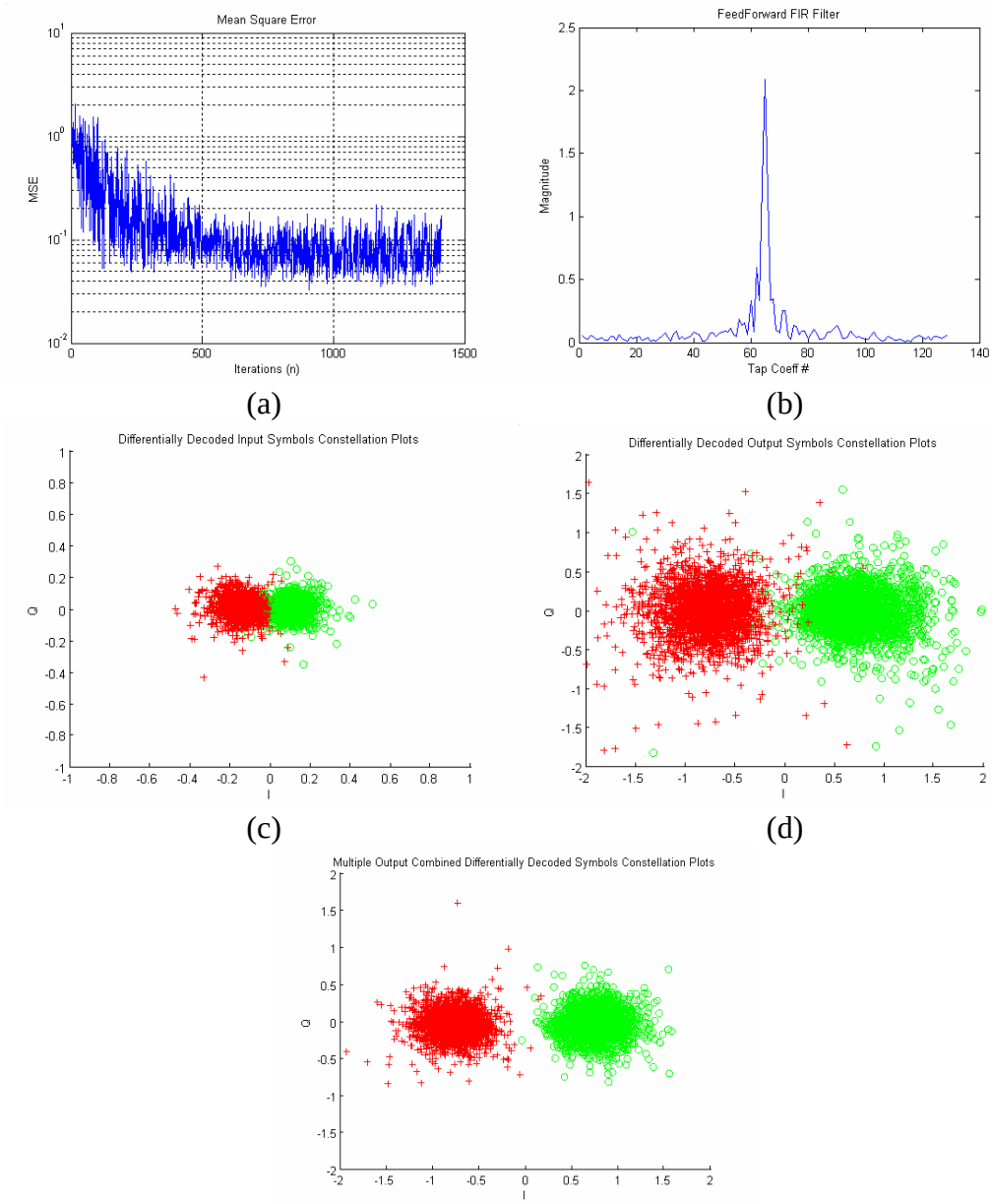

Figure 4-10. Multichannel combining with LE-LMS equalization-distance: 2740m (a) Mean square error (b) Filter tap coefficients (c)Input I-Q plot of differential decoded *r(k)* (d) single channel output I-Q plot of $\tilde{a}(k)$ (e) Multiple channel combined IQ Plot

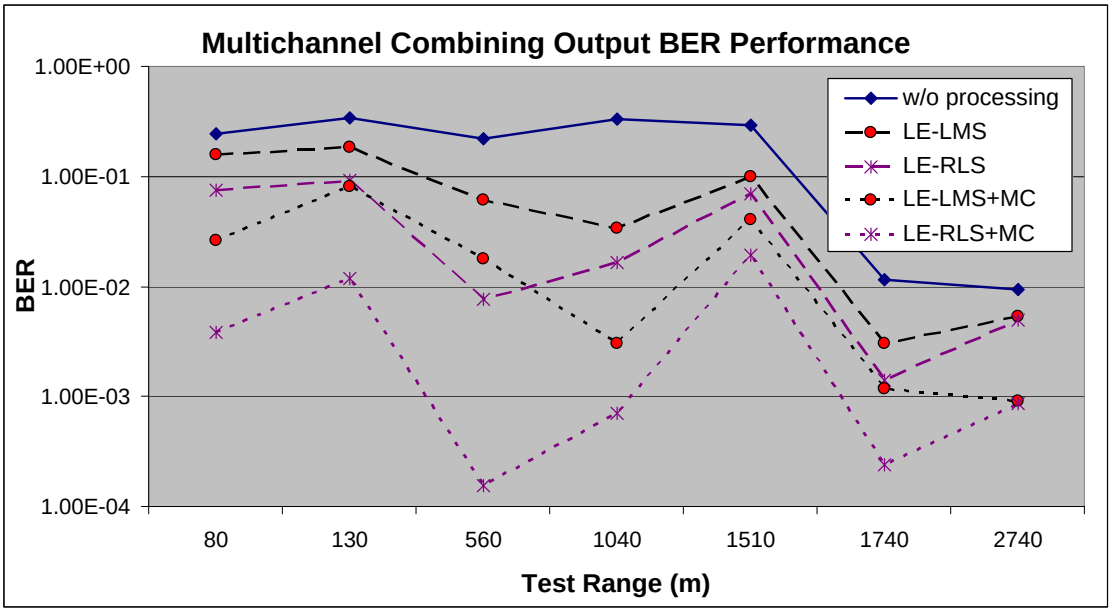

Figure 4-11 BER performances of multichannel combining

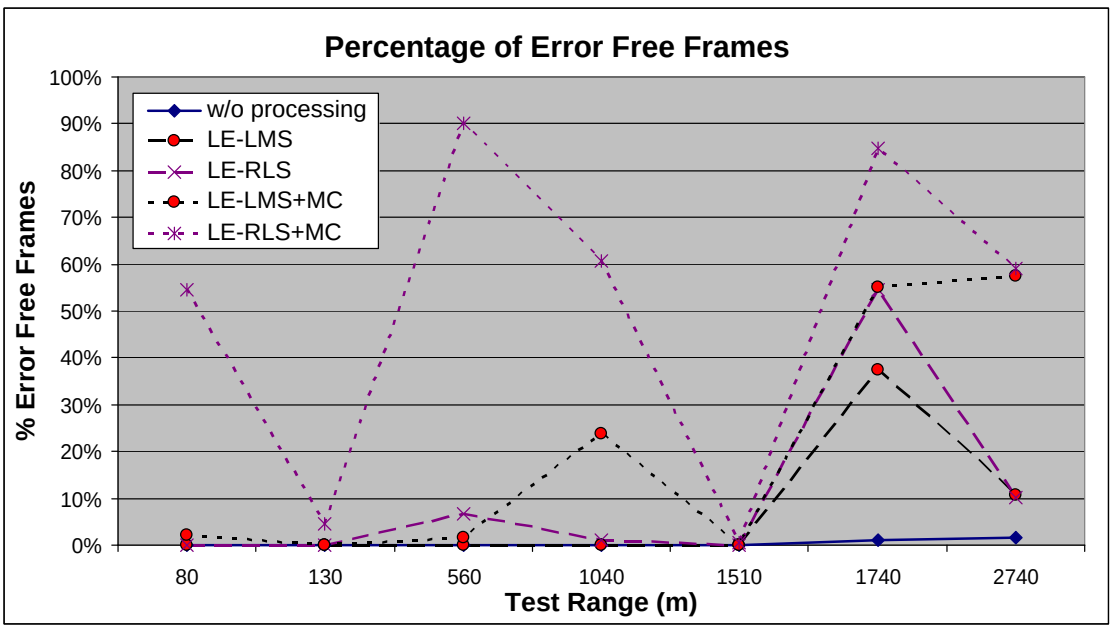

Figure 4-12 Percentage of error free frames after multichannel combining

Table 4-11. Trial BER Results of DBPSK in Shallow Water Channels after LE-LMS and MC

Range (m)	Without Equalization			With LE-LMS		
	Input Error Bits	Input BER	Input FER	Output Error Bits	Output BER	Output FER
80	57391	2.41e-1	1	37647	1.58e-1	1
	55443	2.33e-1	1	36462	1.53e-1	1
	57065	2.40e-1	1	44528	1.87e-1	1
	56429	2.37e-1	1	39569	1.67e-1	1
	58715	2.47e-1	1	38894	1.64e-1	1
	After multichannel combine ->			**6237**	**2.62e-2**	**9.77e-1**
130	81626	3.44e-1	1	43316	1.82e-1	1
	78404	3.30e-1	1	48291	2.03e-1	1
	83224	3.50e-1	1	53828	2.27e-1	1
	80005	3.37e-1	1	49470	2.08e-1	1
	71644	3.02e-1	1	42912	1.81e-1	1
	After multichannel combine ->			**19441**	**8.18e-2**	**1**
560	52450	2.21e-1	1	14457	6.08e-2	1
	53116	2.24e-1	1	17744	7.47e-2	1
	53914	2.27e-1	1	19598	8.25e-1	1
	59470	2.5e-1	1	24331	1.02e-1	1
	50913	2.14e-1	1	17574	7.40e-2	1
	After multichannel combine ->			**4241**	**1.78e-2**	**9.85e-1**
1040	59791	3.36e-1	1	6024	3.38e-2	1
	60625	3.40e-1	1	5966	3.35e-2	1
	64224	3.60e-1	1	6982	3.92e-2	1
	65930	3.70e-1	1	8632	4.84e-2	1
	62179	3.49	1	7293	4.09e-2	1
	After multichannel combine ->			**543**	**3.05e-3**	**7.63e-1**
1510	51465	2.89e-1	1	17561	9.85e-2	1
	49897	2.80e-1	1	17794	9.99e-2	1
	44840	2.52e-1	1	18775	1.05e-1	1
	54025	3.03e-1	1	19689	1.10e-1	1
	49952	2.80e-1	1	20436	1.15e-1	1
	After multichannel combine ->			**7304**	**4.10e-2**	**1**
1740	2047	1.15e-2	9.90e-1	542	3.04e-3	6.26e-1
	2391	1.34e-2	9.80e-1	1396	7.83e-3	9.14e-1
	4312	2.42e-2	1	993	5.57e-3	8.23e-1
	3726	2.09e-2	1	2214	1.24e-2	9.80e-1
	6736	3.78e-3	1	1606	9.01e-3	9.34e-1
	After multichannel combine ->			**210**	**1.18e-3**	**4.49e-1**
2740	1681	9.43e-3	9.85e-1	955	5.36e-3	8.93e-1
	1394	7.82e-3	9.75e-1	916	5.14e-3	8.64e-1
	1246	6.99e-3	9.60e-1	758	4.25e-3	8.84e-1
	1677	9.41e-3	9.85e-1	759	4.26e-3	8.59e-1
	2562	1.44e-3	9.95e-1	1138	6.39e-3	9.39e-1
	After multichannel combine ->			**161**	**9.03e-4**	**4.24e-1**

Table 4-12. Trial BER Results of DBPSK in Shallow Water Channels after LE-RLS and MC

Range (m)	Without Equalization			With LE-LMS		
	Input Error Bits	Input BER	Input FER	Output Error Bits	Output BER	Output FER
80	57391	2.41e-1	1	17863	7.52e-2	1
	55443	2.33e-1	1	16270	6.85e-2	1
	57065	2.40e-1	1	19391	8.16e-2	1
	56429	2.37e-1	1	18284	7.70e-2	1
	58715	2.47e-1	1	19859	8.36e-2	1
	After multichannel combine ->			**900**	**3.78e-3**	**4.55e-1**
130	81626	3.44e-1	1	22056	9.28e-2	1
	78404	3.30e-1	1	25154	1.02e-1	1
	83224	3.50e-1	1	23896	1.00e-1	1
	80005	3.37e-1	1	25366	1.07e-1	1
	71644	3.02e-1	1	21843	9.19e-2	1
	After multichannel combine ->			**2794**	**1.18e-2**	**9.55e-1**
560	52450	2.21e-1	1	1828	7.69e-3	9.32e-1
	53116	2.24e-1	1	1832	7.71e-3	9.32e-1
	53914	2.27e-1	1	2286	9.62e-3	9.66e-2
	59470	2.5e-1	1	3590	1.51e-2	9.70e-2
	50913	2.14e-1	1	4407	1.85e-2	9.92e-2
	After multichannel combine ->			**37**	**1.56e-4**	**9.85e-2**
1040	59791	3.36e-1	1	2920	1.64e-2	9.90e-1
	60625	3.40e-1	1	2660	1.49e-2	9.85e-1
	64224	3.60e-1	1	3513	1.97e-2	1
	65930	3.70e-1	1	4142	2.32e-2	1
	62179	3.49	1	3756	2.10e-1	1
	After multichannel combine ->			**126**	**7.07e-4**	**3.94e-1**
1510	51465	2.89e-1	1	12506	7.02e-2	1
	49897	2.80e-1	1	11485	6.43e-2	1
	44840	2.52e-1	1	13151	7.38e-2	1
	54025	3.03e-1	1	12830	7.20e-2	1
	49952	2.80e-1	1	15934	8.94e-2	1
	After multichannel combine ->			**3416**	**1.92e-2**	**9.94e-1**
1740	2047	1.15e-2	9.90e-1	252	1.41e-3	4.55e-1
	2391	1.34e-2	9.80e-1	328	1.84e-3	6.06e-1
	4312	2.42e-2	1	260	1.46e-3	4.90e-1
	3726	2.09e-2	1	442	2.48e-3	6.41e-1
	6736	3.78e-3	1	434	2.44e-3	6.57e-1
	After multichannel combine ->			**43**	**2.41e-4**	**1.52e-1**
2740	1681	9.43e-3	9.85e-1	889	4.99e-3	8.99e-1
	1394	7.82e-3	9.75e-1	815	4.57e-3	8.54e-1
	1246	6.99e-3	9.60e-1	707	3.97e-3	8.54e-1
	1677	9.41e-3	9.85e-1	721	4.04e-3	8.38e-1
	2562	1.44e-3	9.95e-1	1013	5.68e-3	9.29e-1
	After multichannel combine ->			**155**	**8.70e-4**	**4.09e-1**

4.10 Channel Coding

Turbo codes and the associated iterative decoding techniques have generated much interest within the research fraternity in recent years for their ability to achieve an exceptionally low BER with a signal to noise ratio per information bit close to Shannon's theoretical limit on a Gaussian channel [46]. Turbo Product Code (TPC) was selected as the FEC due to its powerful error-correction capability based on soft-input-soft-output (SISO) iterative decoding algorithm and its excellent BER performance at high code rate (> 0.65) [47]. Implementation-wise, TPCs are less complex than Berrou's turbo convolutional codes, with the Chase Algorithm simplifying the decoding effort required for TPCs [48].

The TPC encoder structure is illustrated in Figure 4-13. For TPC encoding, a total of 676 information bits are placed into a $k_u \times k_u$ array. Then a single-parity-check code is applied to every row of the array to result in a $k_u \times n_d$ matrix and subsequently the same code is applied to every column of the resultant matrix to yield an $n_d \times n_d$ matrix that contains 900 bits (a so-called product code). The code rate is $k_u^2/n_d^2 \approx 0.75$. For DQPSK modulation, each OFDM frame contains two TPC code blocks; and for DBPSK modulation, each OFDM frame contains just one TPC code block.

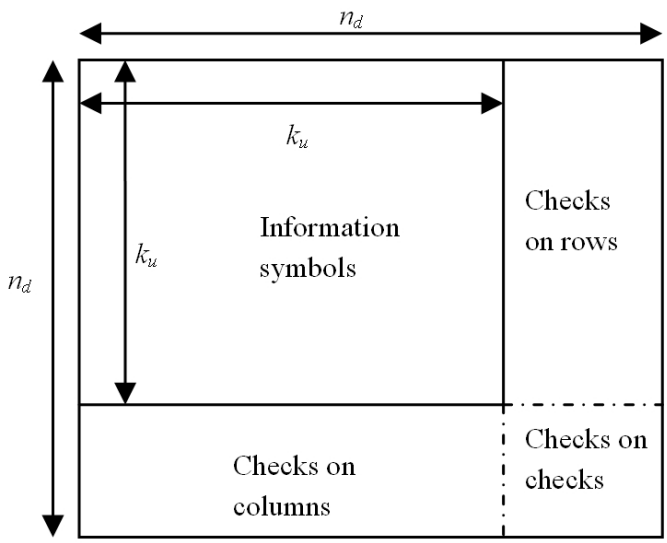

Figure 4-13. Turbo product code (TPC) encoder structure

The TPC decoding is based on soft-input soft-output iterative algorithms and the details can be found in [47].

Although the data in the DBPSK frame format is uncoded, the channel effect encountered in the received trial data can be extracted from the combined *y(k)* in Figure 4-9 and ported over to a TPC codeword. This was done by the following method on the data segment of *y(k)*:

1. Channel effect extraction

$$c_e(k) = \frac{y(k)}{d(k)} \qquad \textbf{(Eq. 4-47)}$$

2. Porting channel effect to differentially encoded TPC codeword $d_c(k)$

$$y_c(k) = d_c(k)c_e(k) \qquad \textbf{(Eq. 4-48)}$$

where $d_c(k) = a_c(k)d_c(k-1)$ and $a_c(k)$ is the TPC codeword.

This is done assuming that:

$$y(k) = d_y(k)e^{j\phi} + n(k) \qquad \textbf{(Eq. 4-49)}$$

where $d_y(k)$ is the scaled version of $d(k)$, ϕ is the single value constant phase offset and $n(k)$ is the noise. This is done for all the distances' data set and their BERs and FERs have been computed and found to be the same as the original data in table 8, as expected. The coding performance are computed and tabulated in Table 4-13 and Table 4-14.

Figure 4-14 and Figure 4-15, gives an overview on the performance enhancements over the different schemes applied. Finally, with LE-LMS, MC, and TPC, more than 75% of the frames received were error free at most distances. At distances of 1040m, 1740m and 2740m, all coded frames received were 99%-100% recovered with no errors. The performance of 140m and 1510m were considered poor. These may be caused by fading effects that the LMS equalizers were not fast enough

compensate. However, with the LE-RLS, MC, and TPC, it could adapt to the channel more quickly. More than 97% of the frames received were error free at all distances. At distances of 560m, 1040m and 1740m, all coded frames received were 100% recovered with no errors. The BER of LE-RLS, MC and TPC was also much better than the LMS case, especially in the shorter ranges.

Table 4-13. Trial BER Results of DBPSK in Shallow Water Channels after LE-LMS, MC and TPC

Range (m)	No. of frames	Error bits	BER	FER
80	264	2006	1.12e-2	1.74e-1
130	264	14356	8.04e-2	7.12e-1
560	264	476	2.67e-3	6.06e-2
1040	198	0	<7.47e-6	<5.05e-3
1510	198	1831	1.37e-2	2.58e-1
1740	198	0	<7.47e-6	<5.05e-3
2740	198	5	3.75e-5	5.05e-3

Table 4-14. Trial BER Results of DBPSK in Shallow Water Channels after LE-RLS, MC and TPC

Range (m)	No. of frames	Error bits	BER	FER
80	264	89	4.99e-4	2.27e-2
130	264	138	7.73e-4	1.51e-2
560	264	0	<5.60e-6	<3.79e-3
1040	198	0	<7.47e-6	<5.05e-3
1510	198	129	9.64e-4	3.03e-2
1740	198	0	<7.47e-6	<5.05e-3
2740	198	4	2.99e-5	5.05e-3

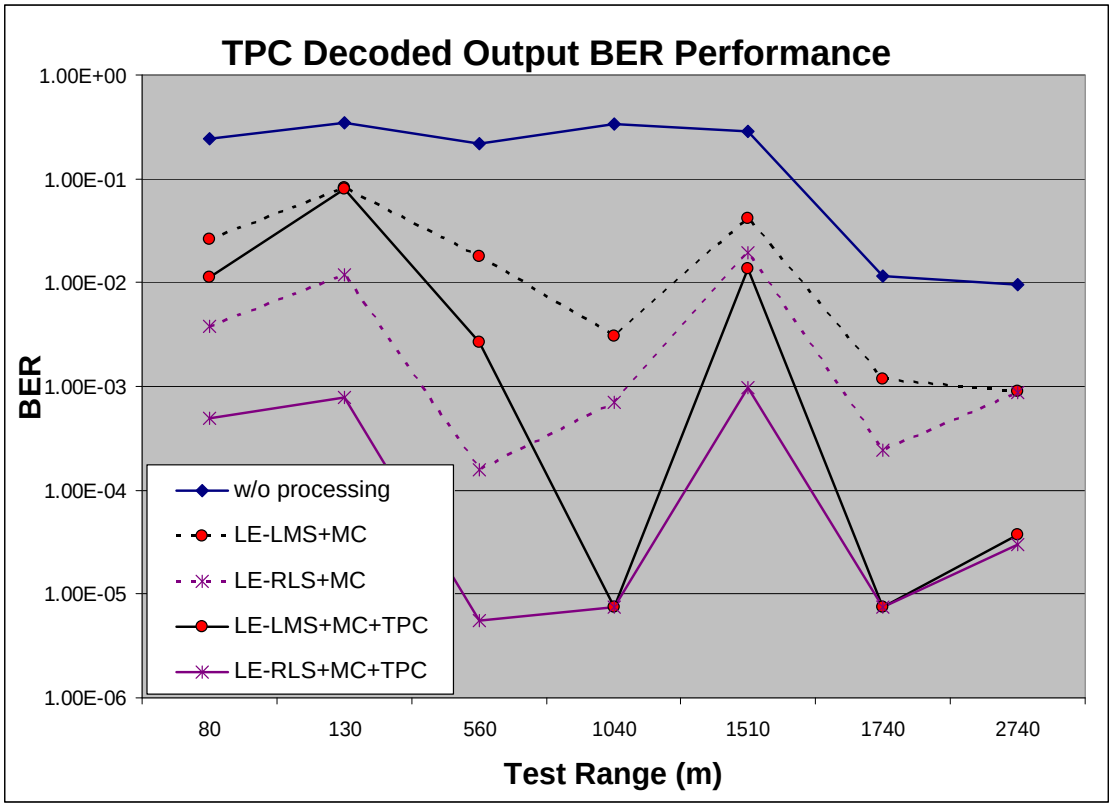

Figure 4-14 BER performances of different schemes

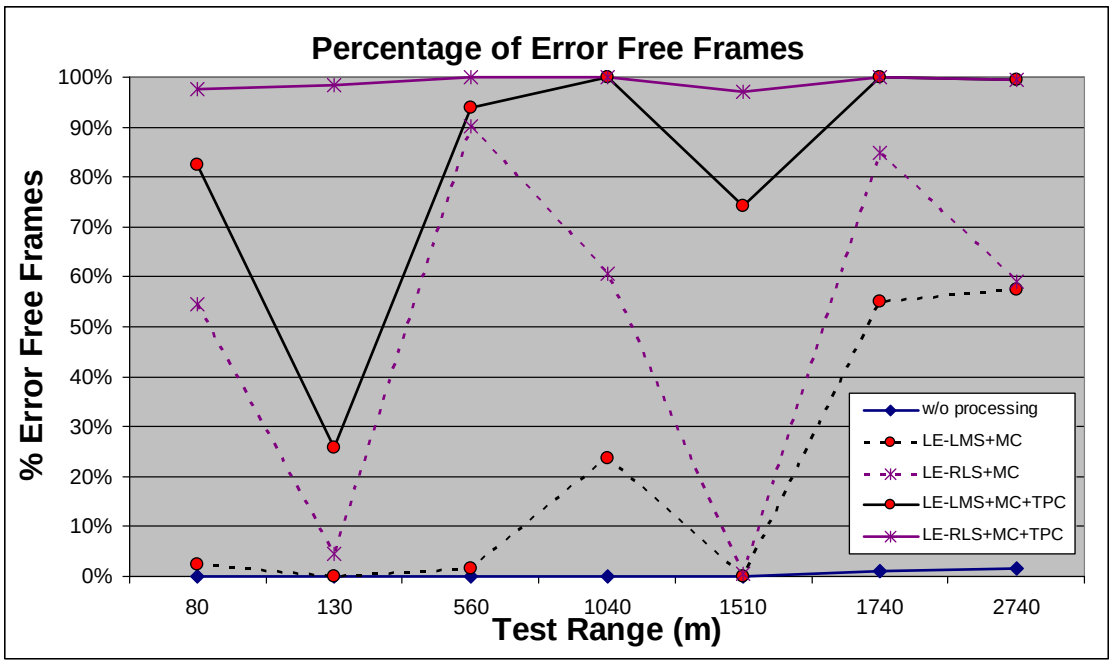

Figure 4-15. Error-free frame performances of different schemes

CHAPTER 5 CONCLUSION

This thesis studied the local shallow water characteristics and presented a communication channel model simulation for the above measured channel environment. Rayleigh fading was observed at shorter distances and Ricean fading occurred in the longer distances. The delay and Doppler effects were also less at longer distances. Ambient noise measured was non-Gaussian with a heavy tailed distribution. The communication channel simulator in this thesis was verified to be a good approximation to the real shallow water channel. Communication engineers should exploit the channel characteristics at longer distances to transmit at higher data rates. On the other hand, it would be a serious challenge to design a modem for shorter distances. This was due to increased fading, delay and Doppler spreads at shorter distances. To combat these effects, a combination of adaptive equalization, multichannel combining (MC) and forward error correction (FEC) were used. In addition, sparse equalization was used and it did not improve the BER performance significantly. It was noted that the BER performance of adaptive linear equalizer (LE) was generally better than decision feedback equalizer (DFE) for shorter distances. The RLS algorithm also performed better than the LMS algorithm with faster convergence rate and less noise. FEC scheme such as turbo product codes (TPC) are employed to improve performance by removing correctable errors and increasing the number of error free frames. Because of LMS simplicity and ease of implementation, both LE-LMS and LE-RLS had been processed with MC and FEC. However, with the combined use of linear equalization, multichannel combination and turbo decoding, only the RLS case could produce reliable data reception with of BERs ($\sim 10^{-4}$) and 97%-100% error free frames. After removing the training and coding overheads, the data rate achievable is approximately 6kbps ~BER 10^{-4} for distances of 80m to 2740m.

CHAPTER 6 FUTURE WORK

This thesis had not analysed the performance of coherent PSK. Although this would add complexity to the receiver, it might give a 3-6 dB improvement in the SNR and lower the BER further. As the computational complexity required for reliable communication was found to be high, other lower complexity but fast convergence adaptation algorithms should be explored. Other channel coding schemes might be explored, especially those that allowed feedback to the equalizer. It was noted that the DFE poor performance could be due to unreliable tracking when there was too much bit errors received. Thus by feeding back a more reliable data source such as channel decoded sequence, the DFE performance might improve. Apart from reducing the complexity and improving the BERs, there were at least two more hurdles for a complete underwater acoustic communication solution. Firstly, considering the fact the mobility introduced faster fading and larger Doppler spread, the mobile communication channel would be an even more challenging one than a static channel. As such, channel measurements and modelling for the mobile channel could help the communication engineer to combat these effects. Secondly, higher order of modulation should be explored so that the bandwidth efficiency for the communication link can be increased for a severely band-limited acoustic channel. Some analysis of spatial coherence of the channel should also be done to assess the feasibility of MIMO as MIMO can increase the data rate through space-time diversity.

BIBLIOGRAPHY

[1] E. MacCurdy, *Notebooks of Leonardo Da Vinci*. New York: George Braziller, 1954.

[2] R. Coates, "The SONAR Course," Seiche.com, 2001.

[3] R. Coates, "The Advance SONAR Course," Seiche.com, 2001.

[4] M. Stojanovic, "Recent Advances in High Rate Underwater Acoustic Communications," *IEEE Journal of Oceanic Engineering*, vol. 21, pp. 125-136, April 1996.

[5] J. A. Catipovic, "Perfomance Limitations in Underwater Acoustic Telemetry," *IEEE Journal of Oceanic Engineering*, vol. 15, pp. 205-216, July 1990.

[6] M. Chitre, J. Potter, and S. H. Ong, "Underwater Acoustic Channel Characterization for Medium-range Shallow Water Communication," in *Proceedings of MTS/IEEE TECHNO-OCEANS '04*, 2004, pp. 40-45.

[7] H. V. Poor and G. W. Worndell, *Wireless Communications - Signal Processing Perspective*. New Jersey: Prentice Hall, 1998.

[8] M. Stojanovic, *Underwater Acoustic Digital Signal Processing and Communication Systems*. Boston: Kluwer, 2002.

[9] S. P. Tan, T. B. Koay, P. Venugopalan, M. A. Chitre, and J. R. Potter, "Development of a Shallow Water Ambient Noise Database," in *International Symposium on Underwater Technology 2004*, Taiwan, 2004, pp. 169-173.

[10] A. Zielinski, Y. H. Yoon, and L. Wu, "Performance Analysis of Digital Acoustic Communication in a Shallow Water Channel," *IEEE Journal of Oceanic Engineering*, vol. 20, pp. 293-299, October 1995.

[11] H. K. Yeo, B. S. Sharif, A. E. Adams, and O. R. Hinton, "Analysis of Experimental Shallow Water Network Channel and Theoretical Channel Model," in *Oceans 2000 MTS/IEEE Conference and Exhibition*, Providence, RI, 2000, pp. 2025-2029.

[12] X. Geng and A. Zielinski, "An Eigenpath Underwater Acoustic Communication Channel Model," in *Proceedings of MTS/IEEE Oceans '95*, San Diego, 1995, pp. 1189-1196.

[13] M. A. M. Guitierrez, P. L. P. Sanchez, and J. V. d. V. Neto, "An Eigenpath Underwater Acoustic Communication Channel Simulation," in *Conference Proceedings of MTS/IEEE Oceans 2005*, Washington D. C., 2005, pp. 355-362.

[14] M. Chitre, "Underwater Acoustic Communications in Warm Shallow Water Channels," P.hD. Thesis, Singapore: National University of Singapore, 2006.

[15] T. S. Rappaport, *Wireless Communications*, 2nd ed. New Jersey: Prentice Hall, 2002.

[16] A. H. Quazi and W. L. Konrad, "Underwater Acoustic Communications," *IEEE Communications Magazine*, vol. 20, pp. 24-30, March 1982.

[17] B. A. Tan, S. S. Quek, and N. Zou, "Characterization of Multipath Acoustic Channels in Very Shallow Waters for Communications," in *IEEE Oceans Asia Pacific*, Singapore, 2006.

[18] M. Chitre, S. H. Ong, and J. Potter, "Performance of Coded OFDM in Very Shallow Water Channels and Snapping Shrimp Noise," in *Proceedings of MTS/IEEE Oceans 2005*, Washington D. C., 2005, pp. 996-1001.

[19] K. Zhong, S. S. Quek, T. A. Koh, and B. A. Tan, "A Real-Time Coded OFDM Acoustic Modem in Very Shallow Underwater Commmunications," in *IEEE Oceans Asia Pacific* Singapore, 2006.

[20] J. G. Proakis, *Digital Communications*, 4th ed. New York: Mcgraw Hill, 2001.

[21] B. Farhang-Boroujeny, *Adaptive Filters Theory and Applications*: John Wiley & Sons, 1999.

[22] S. Haykin, *Adaptive Filter Theory*, 4th ed. New Jersey: Prentice Hall, 2002.

[23] M. Stojanovic, J. Catipovic, and J. G. Proakis, "Adaptive Multichannel Combining and Equalization for Underwater Acoustic Communication," *Journal of Acoustic Society of America*, vol. 94, pp. 1621-1631, 1993.

[24] M. Stojanovic and Z. Zvonar, "Multichannel Processing of Broad-Band Multiuser Communication Signals in Shallow Water Acoustic Channels," *IEEE Journal of Oceanic Engineering*, vol. 21, pp. 156-166, April 1996.

[25] V. Capellano, G. Loubert, and G. Jourdain, "Adaptive Multichannel Equalizer for Underwater Communications," in *Proceedings of MTS/IEEE Oceans '96* 1996, pp. 994-999.

[26] H. C. Song, P. Roux, W. S. Hodgkiss, W. A. Kuperman, T. Akal, and M. Stevenson, "Multiple-Input-Multiple-Output Coherent Time Reversal Communications in Shallow-Water Acoustic Channel," *IEEE Journal of Oceanic Engineering*, vol. 31, pp. 170-178, January 2006.

[27] D. B. Kilfoyle, J. C. Preisig, and A. B. Baggeroer, "Spatial Modulation Experiments in the Underwater Acoustic Channel," *IEEE Journal of Oceanic Engineering*, vol. 30, pp. 406-415, Aril 2005.

[28] G. D. Durgin, *Space-Time Wireless Channels*. New Jersey: Prentice Hall, 2003.

[29] M. Kocic, D. Brady, and M. Stojanovic, "Sparse Equalization for Real-Time Digital Underwater Acoustic Communications," in *Proceedings of MTS/IEEE Oceans '95*, 1995, pp. 1417-1472.

[30] N.-I. Heo, D. S. Han, and H.-S. Oh, "Adaptive Sparse Equalizer Robust to Fast Fading and Long Delay Spread for ASTC DTV," *IEEE Transactions on Consumer Electronics,* vol. 51, pp. 803-808, August 2005.

[31] L. M. Brekhovskikh, *Waves in Layered Media*, 1st ed. New York: Academic Press, 1960.

[32] "Acoustic Modelling and Performance Prediction," in *Training Resource Materials*: DSO National Laboratories, 2002.

[33] R. Coates, "An Empirical Formula for Computing the Beckhamn-Spizzichino Surface Reflection Loss Coefficient," *IEEE Transactions on Ultrasonics, Ferroelectric and Frequency Control,* vol. 35, pp. 522-523, July 1988.

[34] R. J. Urich, *Principles of Underwater Sound*, 3rd ed. New York: Mcgraw Hill, 1983.

[35] R. L. Peterson, R. E. Ziemer, and D. E. Borth, *Introduction to Spread Spectrum Communications*, 1st ed. New Jersey: Prentice Hall, 1995.

[36] D. C. Cox, "Delay Doppler Characteristics of Multipath Propagation at 910MHz in a Suburban Mobile Radio Environment," *IEEE Transactions on Antennas and Propagation,* vol. 20, pp. 625-635, September 1972.

[37] M. C. Jeruchim, P. Balaban, and K. S. Shanmugan, *Simulation of Communication Systems*, 2nd ed. New York: Kluwer/Plenum, 2000.

[38] G. Jourdain and J. P. Henrioux, "Use of Large Bandwidth-Duration Binary Phase Shift Keying Signals in Target Delay-Doppler Measurements," *Journal of Acoustic Society of America,* vol. 90, pp. 299-309, July 1991.

[39] E. F. Fama and R. Roll, "Parameter Estimates for Symmetric Stable Distributions," *Journal of American Statistics Association,* vol. 66, pp. 331-338, 1971.

[40] G. Cormode, "Generating Stable Distributions," *http:\\dimacs.rutgers.edu/~graham/code.html,* 2005.

[41] J. P. Nolan, "Stable Distributions Models for Heavy Tailed Data," book in progress-unpublished, 2005.

[42] L. Qin, J. Xiong, W. Zhang, and J. Chen, "Fractionally Spaced Adaptive Decision Feedback Equalizers with Applications to ATSC DTV Receivers," *IEEE Transactions on Consumer Electronics,* vol. 50, pp. 999-1003, November 2004.

[43] J. R. Treichler, I. Fijalkow, and C. R. J. Johnson, "Fractionally Spaced Equalizers - How long should they be?," *IEEE Signal Processing Magazine,* vol. 13, pp. 65-81, May 1996.

[44] M. Stojanovic, "An Adaptive Algorithm for Differentially Coherent Detection in the Presence of Intersymbol Interference " *IEEE Journal on Selected Areas in Communications,* vol. 23, pp. 1884-1890, September 2005.

[45] S. Robert, H. G. Wolfgang, and B. H. Johannes, "Adaptive Linear Equalization Combined with Noncoherent Detection for MDPSK Signals," *IEEE Transactions on Communications,* vol. 48, pp. 733-738, May 2001.

[46] C. Berrou and A. Glavieux, "Near Optimum Error Correcting Coding and Decoding: Turbo Codes " *IEEE Transactions on Communications,* vol. 44, pp. 1261-1271, October 1996.

[47] Pyndiah, "Near-optimum Decoding of Product Codes: Block Turbo Codes," *IEEE Transactions on Communications,* vol. 46, pp. 1003-1010, August 1998.

[48] D. Chase, "Class of Algorithms for Decoding Block Codes with Channel Measurement Information," *IEEE Transactions on Information Theory,* vol. 18, pp. 170-182, January 1972.